

Turing Instability in a Boundary-fed System

S. Setayeshgar* and M. C. Cross

Condensed Matter Physics 114-36, California Institute of Technology, Pasadena, CA 91125

(October 3, 2018)

Abstract

The formation of localized structures in the chlorine dioxide-iodine-malonic acid (CDIMA) reaction-diffusion system is investigated numerically using a realistic model of this system. We analyze the one-dimensional patterns formed along the gradients imposed by boundary feeds, and study their linear stability to symmetry-breaking perturbations (Turing instability) in the plane transverse to these gradients. We establish that an often-invoked simple local linear analysis which neglects longitudinal diffusion is inappropriate for predicting the linear stability of these patterns. Using a fully nonuniform analysis, we investigate the structure of the patterns formed along the gradients and their stability to transverse Turing pattern formation as a function of the values of two control parameters: the malonic acid feed concentration and the size of the reactor in the dimension along the gradients. The results from this investigation are compared with existing experiments.

PACS: 82.20.Wt; 82.20.Mj; 47.54.+r

Typeset using REVTeX

*Corresponding author, Present address: Physics Department, Northeastern University, Email: simas@masto.physics.neu.edu, Fax: 617 373 2943, Telephone: 617 373 2944

I. INTRODUCTION

Recent experimental developments have made possible the study of asymptotic spatiotemporal behavior in chemical systems in a controlled and reproducible manner, allowing predictions from theoretical and numerical studies of these systems to be compared quantitatively with experiments, in the same way that fluid systems have been studied. Indeed, the understanding of spatial pattern formation in nonequilibrium systems has greatly benefited from careful and controlled experiments on fluid systems [1]. Unlike fluid systems which at high nonlinearity break down to a turbulent state characterized by a wide range of spatial scales, spatial patterns in chemical systems can be studied at high nonlinearity [2], thus providing an opportunity to study rich and new phenomena that complement our knowledge from pattern formation in fluid systems.

The symmetry-breaking instability of a system from a homogeneous state to a patterned state, predicted in 1952 by Alan Turing [3], was observed for the first time nearly 40 years later, in the chlorite-iodide-malonic acid (CIMA) reaction-diffusion system [4–6]. The Turing instability is characterized by an intrinsic wavelength resulting solely from reaction and diffusion processes. For this reason, it has particular relevance to pattern formation in biological systems [7].

In contrast to hydrodynamic systems for which the governing equations and parameter values are well understood, how to model complex chemical systems is often not well known [1]. A realistic model of the simpler chlorine dioxide-iodine-malonic acid (CDIMA) reaction, which is similar to the CIMA reaction in terms of its stationary pattern-forming and dynamical behavior, has been proposed by Lengyel, Rabai and Epstein (henceforth referred to as LRE) [8,9]. Hence, the CDIMA reaction-diffusion system has the potential to become an archetype for the study of nonequilibrium pattern formation [10] in chemical systems, in principle allowing numerical and theoretical investigations to be compared directly with experiments.

In practice, however, this has not been fully realized for two reasons. First, numerical investigations of reaction-diffusion equations using realistic chemical parameters is a demanding computational task. In addition, the algebraic complexity of the realistic nonlinear reaction terms renders these models unsuitable for analysis by standard analytical tools. As a result, the theoretical work on reaction-diffusion systems has been mostly based on abstract models. Second, despite the existence of the realistic CDIMA chemical model which has similar pattern-forming and dynamical properties to the related CIMA system, experimental work has continued to be based on the CIMA reaction, making direct comparisons of numerical and analytical work with experiments difficult. Consequently, unlike in fluid systems, experimental and theoretical efforts in chemical systems have not been closely coupled.

In this article, we use the realistic LRE model of the CDIMA reaction-diffusion system to investigate the Turing instability numerically [11]. Contrary to the case originally considered by Turing and subsequently by others, the experimental conditions under which Turing patterns form are not uniform, as required by the continuous feed of reservoir chemicals. We study the formation and stability of one-dimensional structures in the presence of boundary feed gradients. We first briefly review the Turing mechanism in Section II. To facilitate comparisons with our numerical investigations, we describe the geometry and setup employed

by the relevant experiments in Section III. The LRE chemical model is described in Section IV. In Section V A, we obtain the one-dimensional steady state chemical concentration profiles for a particular set of boundary conditions, and explore several different approaches to determine the linear stability of these profiles to transverse symmetry-breaking patterns. In Section V B, the patterns along the gradients and their linear stability are further explored as a function of two control parameters. We summarize our results and consider prospects for further progress in Section VI.

II. TURING INSTABILITY CONDITIONS

In his original paper [3], Turing suggested that the reaction and diffusion of chemicals could account for the instability of an originally homogeneous steady state to a stable steady pattern when triggered by random disturbances. These instability conditions, which are derived and discussed in detail in the text by Murray [7] are presented here for the purpose of introducing the notation for the rest of the article. Consider the general governing equations for the reaction-diffusion mechanism of two chemical species:

$$\sigma \frac{\partial u}{\partial t} = f(u, v; \vec{\mu}) + \nabla^2 u \quad (1)$$

$$\frac{\partial v}{\partial t} = g(u, v; \vec{\mu}) + c \nabla^2 v, \quad (2)$$

where f and g represent the (nonlinear) reaction kinetics, u and v are chemical concentrations, $\vec{\mu}$ is a set of reaction parameters that may include concentrations of other chemical species, $c = D_v/D_u$ is the ratio of diffusion constants, and $\sigma \geq 1$ is a constant separating the characteristic time scales for changes in the concentrations of the u and v species. Turing's idea was as follows [7]: if in the absence of diffusion ($u(\vec{r}, t), v(\vec{r}, t)$) tend to a linearly stable uniform steady state, then under certain conditions, the addition of diffusion leads to the development of spatially inhomogeneous patterns. Although these conditions were originally considered for a spatially uniform system, where the parameters $\vec{\mu}$ are constant, the actual experimental realization of the Turing instability occurs in the presence of externally imposed feed gradients, where $\vec{\mu} = \vec{\mu}(z)$. In this section, we derive the Turing *linear* instability conditions for both uniform and nonuniform parameters, $\vec{\mu}$.

A. Uniform background

The uniform background case is realized experimentally in batch reactors where there are no externally imposed gradients from continuous feed of chemical reactants, and Turing patterns are necessarily transient. The parameters $\vec{\mu}$ are constants independent of position. The homogeneous steady state $\vec{c}_s = (u_s^o, v_s^o)$ is obtained as the solution to:

$$f(u, v; \vec{\mu}) = g(u, v; \vec{\mu}) = 0. \quad (3)$$

The linear stability of this state is obtained by substituting into the governing reaction-diffusion equations:

$$\vec{c}(\vec{r}, t) = \vec{c}_s + \delta\vec{c}(\vec{r}, t), \quad (4)$$

$$\delta\vec{c}(\vec{r}, t) = \sum_k (\delta u_k^o, \delta v_k^o) e^{i\vec{k}\cdot\vec{r}} e^{\lambda_k t}, \quad (5)$$

where $\vec{c} = (u, v)$ is a vector of concentrations, k is the spatial wave number of the perturbation, λ_k is the growth rate of the k^{th} mode, and $(\delta u_k^o, \delta v_k^o)$ is the corresponding constant eigenvector. The resulting linear eigenvalue problem:

$$\begin{pmatrix} (a_{11} - k^2)/\sigma & a_{12}/\sigma \\ a_{21} & a_{22} - ck^2 \end{pmatrix} \begin{pmatrix} \delta u_k^o \\ \delta v_k^o \end{pmatrix} = \lambda_k \begin{pmatrix} \delta u_k^o \\ \delta v_k^o \end{pmatrix} \quad (6)$$

yields,

$$\lambda_k^{(\pm)} = -\frac{1}{2\sigma} [(\sigma c + 1)k^2 - (a_{11} + \sigma a_{22})] \pm \frac{1}{2\sigma} \sqrt{[(\sigma c + 1)k^2 - (a_{11} + \sigma a_{22})]^2 - 4h(k^2)}, \quad (7)$$

where

$$h(k^2) = \sigma [ck^4 - (a_{22} + ca_{11})k^2 + (a_{11}a_{22} - a_{12}a_{21})]. \quad (8)$$

The quantities $a_{11} = f_u$, $a_{12} = f_v$, $a_{21} = g_u$, and $a_{22} = g_v$ are the elements of the Jacobian of the reaction terms with respect to the concentrations, evaluated at the uniform steady state. λ_k has a rich behavior depending on the values of σ , c , and a_{ij} . The conditions for the Turing instability are that this uniform steady state be linearly: (i) stable to homogeneous perturbation, and (ii) unstable to inhomogeneous perturbations. Hence, this is a *symmetry-breaking* mechanism, since it breaks the homogenous spatial symmetry of the uniform state. For the general reaction-diffusion system given in Eqs. (1) and (2), these conditions are derived in Appendix A. Below, we refer to the relevant results for the purpose of discussion. Stability of the uniform steady state to homogeneous $k = 0$ perturbations requires the following inequalities to be satisfied:

$$a_{11} + \sigma a_{22} < 0, \quad (9)$$

$$a_{11}a_{22} - a_{12}a_{21} > 0. \quad (10)$$

In order for the uniform steady state to be simultaneously unstable to inhomogeneous $k \neq 0$ perturbations, we must have

$$a_{22} + ca_{11} > 0, \quad (11)$$

$$(a_{22} + ca_{11})^2 - 4c(a_{11}a_{22} - a_{12}a_{21}) \geq 0. \quad (12)$$

Comparing Eqs. (9) and (11) we conclude that a_{11} and a_{22} must have opposite sign. In the standard terminology, the activator species has a positive sign and the inhibitor has a negative sign in the Jacobian. Thus, taking $a_{11} > 0$ and $a_{22} < 0$ identifies u as the activator and v as the inhibitor. If $\sigma = 1$, then Eqs. (9) and (11) are simultaneously satisfied only for $c > 1$. In fact, given values of other parameters, $c \gg 1$ is required. Since diffusion constants

of ions in aqueous solutions are all nearly the same ($\mathcal{O}(10^{-5})\text{cm}^2\text{s}^{-1}$), for the instability conditions to be satisfied, σ must be greater than one. In Section IV, the requirement $\sigma > 1$ will be put in the context of the fortuitous role of the starch color indicator in the pattern formation itself by providing the mechanism for slowing the activator reaction and diffusion with respect to those of the inhibitor.

Equations (9)–(12) constitute the Turing conditions. It will be useful for future comparison of the local stability analysis with the full stability analysis of the nonuniform steady state to consider the Hopf bifurcation of the uniform system. For reaction parameters such that

$$(a_{11} - \sigma a_{22})^2 + 4\sigma a_{12}a_{21} < 0, \quad (13)$$

there will be a complex conjugate pair of eigenvalues for wave numbers in the range $0 < k^2 < k_+^{(\text{H})2}$, where $k_+^{(\text{H})2}$ is given in Eq. (A12). With the above inequality satisfied, a Hopf bifurcation of the uniform system occurs when $(a_{11} + \sigma a_{22}) > 0$. Beyond the Hopf bifurcation point, there will be an unstable complex conjugate pair of eigenvalues for wave numbers in the range given by Eq. (A17).

B. Nonuniform background

In this case, the parameters $\vec{\mu}$, which depend on the concentrations of background chemicals fed through the boundaries, are not constant but rather are functions of the variable z along the direction perpendicular to the feed boundaries. The steady state solution will now be a function of z , satisfying:

$$f(u_s(z), v_s(z); \vec{\mu}(z)) + \frac{d^2 u_s}{dz^2} = 0, \quad (14)$$

$$g(u_s(z), v_s(z); \vec{\mu}(z)) + c \frac{d^2 v_s}{dz^2} = 0, \quad (15)$$

with Dirichlet boundary conditions at $z = 0$ and $z = L_z$. The stability of $(u_s(z), v_s(z))$ is given by linearizing about this state:

$$\vec{c}(\vec{r}, t) = \vec{c}_s(z) + \delta\vec{c}(\vec{r}, t), \quad (16)$$

$$\delta\vec{c}(\vec{r}, t) = \sum_{k_\perp} (\delta u_{k_\perp}(z), \delta v_{k_\perp}(z)) e^{i\vec{k}_\perp \cdot \vec{r}_\perp} e^{\lambda_{k_\perp} t}, \quad (17)$$

where \vec{k}_\perp is the wave vector perpendicular to the direction of the gradients. For simplicity of notation, we will drop the subscript “ \perp ,” taking k to be the transverse wave number. The resulting eigenvalue problem is:

$$\begin{pmatrix} \left(a_{11}(z) + \frac{\partial^2}{\partial z^2} - k^2 \right) / \sigma & a_{12}(z) / \sigma \\ a_{21}(z) & a_{22}(z) + c \frac{\partial^2}{\partial z^2} - ck^2 \end{pmatrix} \begin{pmatrix} \delta u_k(z) \\ \delta v_k(z) \end{pmatrix} = \lambda_k \begin{pmatrix} \delta u_k(z) \\ \delta v_k(z) \end{pmatrix}, \quad (18)$$

with $(\delta u_k(z), \delta v_k(z))$ satisfying the same Dirichlet boundary conditions as the steady state. As Pearson *et al.* [12] have noted, this is an infinite-dimensional eigenvalue problem for

each k which is formally similar to the Schrödinger equation. However, the Jacobian of the reaction terms is not symmetric, rendering the linear operator non-Hermitian. Hence, it must be solved numerically, by discretizing the z spatial direction into N_z mesh points and solving the resulting $2N_z \times 2N_z$ matrix eigenvalue problem for each k . This method of solution is described in Section V A 3.

C. Locally uniform background

In the presence of ramps in control parameters, a naive assumption is that a structure will form in the region of space where the local value of the control parameter allows it to be stable in the corresponding uniform problem [15]. This “locally uniform” approach amounts to treating each location along the gradients in the z -direction to be an independent and uniform quasi-two-dimensional system in the $x - y$ plane. The corresponding locally uniform steady state which depends parametrically on z is given by the solution to:

$$f(u, v; \vec{\mu}(z)) = g(u, v; \vec{\mu}(z)) = 0. \quad (19)$$

The Turing instability conditions can then be examined at each point in z to determine whether or not a linear analysis predicts the formation of transverse Turing patterns in any interval along z .

Since the resulting eigenvalue problem for the stability of the locally homogeneous steady state to a symmetry-breaking instability requires only a 2×2 analysis at each z , it is computationally simple. The validity of this local analysis is assessed in Sec. V A 2, by comparing the result with that from the fully nonuniform analysis (Eq. 18) of the steady state along the gradients.

III. EXPERIMENTAL GEOMETRY

The first experimental realization of the steady-state Turing patterns predicted in 1952 was made in 1990 by Castets *et al.* [4], and was subsequently confirmed by others [5,6]. This was made possible by the development of open spatial reactors which allowed experimentalists to maintain a reaction far from equilibrium through a continuous supply of reactants, while avoiding convective transport. These sustained patterns have been obtained in only one controlled experimental system to date, the chlorite-iodide-malonic acid (CIMA) chemical reaction-diffusion system. The principles of operation of these reactors have been discussed elsewhere in detail [4,5,13,14].

In this section, we introduce the thin-strip reactor which is investigated numerically in this work, since a geometrical description of the experimental setup is useful in the understanding of our results. A detailed description of the chemical model is presented later in Section IV, and is not necessary for the discussion presented here. The thin strip reactor is comprised of a thin rectangular gel strip, such that $L \gg w > h$, as in Figure 1. Typically, $h < 1$ mm, $L \sim 25$ mm, and $w \sim 3$ mm. The gels are water-based, acting as essentially water in a loose polymer grid. The gel core of the reactor is in contact with two continuously stirred reservoirs of chemicals. Components of the reaction are distributed in the two reservoirs in such a way that neither is separately reactive. In the CIMA experiments, these reservoir

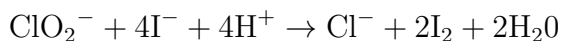
species are malonic acid ($\text{CH}_2(\text{COOH})_2$ or MA), iodide (I^-) and chlorite (ClO_2^-). The LRE model of the CDIMA system takes as input malonic acid, iodine (I_2) and chlorine dioxide (ClO_2). As the reservoir species diffuse and react through the gel, the two dynamical species, iodide and chlorite, which take part in the pattern-forming instability, are produced. The gel is preloaded with a soluble starch that acts as an indicator by changing color from yellow to purple with changes in triiodide concentration. The large starch molecules are immobilized in the gel matrix, and for this reason actually play a role in the pattern formation itself.

Observations are made in the direction perpendicular to the $x-z$ plane (along Oy), which allows viewing of the multfront patterns that develop along the boundary feed gradients (in the z -direction), as well as patterns that form parallel to the boundaries (in the x -direction), breaking the boundary feed symmetry (single or multiple layers of spots). The symmetry-breaking patterns form in a thickness Δ along z . If the gel is thin enough ($h \sim \lambda$ of the Turing patterns), these patterns are one- or two-dimensional, depending on whether Δ is of the order of one or more wavelengths λ of the structure. With $h \gg \lambda$, for example $h \sim L$ as is the case with disc reactors, the patterns are quasi-two-dimensional (referred to as “monolayers”) for $\Delta \sim \lambda$, or three-dimensional for $\Delta \geq \lambda$ (referred to as “bilayers” for $\Delta \sim 2\lambda$).

A modified thin-strip reactor, where the feed surfaces ($L \times h$) are no longer parallel but make an angle, has been developed and used by Dulos *et al.* [14], where $h = 0.2$ mm, $L = 25$ mm, and the w ranges from 1.75 to 3.5 mm. The variation in w causes a gradual change in the reservoir concentration ramps across the gel, the effect of which can be studied on the patterns that form along and transverse to the gradients.

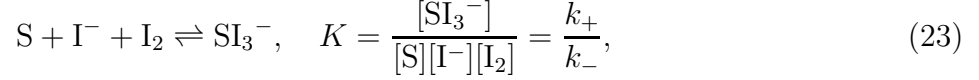
IV. CHEMICAL MODEL OF THE CDIMA SYSTEM

Lengyel, Epstein and Rabai have proposed a model for the temporal oscillations in the chlorite-iodide-malonic acid reaction, ClO_2^- - I^- -MA, which is based on the simpler chlorine dioxide-iodine-malonic acid reaction, ClO_2 - I_2 -MA, referred to as CDIMA [8,9]. They have shown experimentally that the CDIMA system also exhibits the Turing instability in both closed and open systems [16,21]. By monitoring the CIMA reaction in a closed system spectrophotometrically, it was determined that after an initial fast consumption of I^- and ClO_2^- during a pre-oscillatory period to produce I_2 and ClO_2 , the reaction of ClO_2 , I_2 and MA accounts for the oscillations. The LRE CDIMA model consists of three reactions for MA, I_2 , ClO_2 , I^- , ClO_2^- and H^+ [17], with empirically determined rate laws:



$$-\frac{d[\text{ClO}_2^-]}{dt} = k_{3a}[\text{ClO}_2^-][\text{I}^-][\text{H}^+] + \frac{k_{3b}[\text{ClO}_2^-][\text{I}_2][\text{I}^-]}{h + [\text{I}^-]^2} \equiv r_3. \quad (22)$$

Lengyel *et al.* [18] have modeled the effect of unreactive starch-complex formation on the CDIMA system, where the complexing agent is $(\text{S} + \text{I}_2)$. Although formation of the starch-triiodide complex (SI_3^-) is a complicated process, it can nevertheless be described as a single reaction:



where K is the equilibrium constant, and the reaction rate is given by:

$$r_4 \equiv k_+[\text{S}][\text{I}_2][\text{I}^-] - k_-[\text{SI}_3^-]. \quad (24)$$

Using the above, the full reaction-diffusion model for the CDIMA system, with the addition of the reaction with starch, is given by [17]:

$$\frac{\partial[\text{MA}]}{\partial t} = -r_1 + D_{\text{MA}}\nabla^2[\text{MA}] \quad (25)$$

$$\frac{\partial[\text{I}_2]}{\partial t} = -r_1 + \frac{1}{2}r_2 + 2r_3 - r_4 + D_{\text{I}_2}\nabla^2[\text{I}_2] \quad (26)$$

$$\frac{\partial[\text{ClO}_2]}{\partial t} = -r_2 + D_{\text{ClO}_2}\nabla^2[\text{ClO}_2] \quad (27)$$

$$\frac{\partial[\text{I}^-]}{\partial t} = r_1 - r_2 - 4r_3 - r_4 + D_{\text{I}^-}\nabla^2[\text{I}^-] \quad (28)$$

$$\frac{\partial[\text{ClO}_2^-]}{\partial t} = r_2 - r_3 + D_{\text{ClO}_2^-}\nabla^2[\text{ClO}_2^-] \quad (29)$$

$$\frac{\partial[\text{SI}_3^-]}{\partial t} = r_4 \quad (30)$$

$$\frac{\partial[\text{H}^+]}{\partial t} = r_1 - 4r_3 + D_{\text{H}^+}\nabla^2[\text{H}^+]. \quad (31)$$

The rate and diffusion constants used in the numerical calculations here are taken from Refs. [17,19,20] and are given in Table I.

Lengyel *et al.* [8] have shown that these reactions successfully simulate the temporal behavior of $[\text{MA}]$, $[\text{I}_2]$, $[\text{ClO}_2]$, $[\text{I}^-]$, and $[\text{ClO}_2^-]$ in a batch experimental system. Their numerical results show that while the intermediates $[\text{I}^-]$ and $[\text{ClO}_2^-]$ vary by several orders of magnitude during an oscillation, $[\text{MA}]$, $[\text{I}_2]$ and $[\text{ClO}_2]$ vary more slowly. In addition, the contribution of $[\text{H}^+]$ to the reaction terms is relatively small, and this species can be neglected. This suggests a reduction of the full model to a three-variable system ($[\text{I}^-]$, $[\text{ClO}_2^-]$ and $[\text{SI}_3^-]$) by treating the concentrations of the $[\text{MA}]$, $[\text{I}_2]$ and $[\text{ClO}_2]$ reactants as constants, making the model mathematically and numerically more tractable. This procedure illustrates the adiabatic elimination of fast modes in dynamical systems which reduces the full dynamics to only a few degrees of freedom.

It is further assumed that there is a large excess of starch uniformly distributed so that its concentration is always very close to its initial value $[\text{S}]_0$, and that the complex formation and dissociation is fast. Then,

$$[\text{SI}_3^-] \approx K[\text{S}][\text{I}_2] \cdot [\text{I}^-] \approx K'[\text{I}^-], \quad (32)$$

where $K' \equiv K[\text{S}]_o[\text{I}_2]_o$. Adding Eqs. (28) and (30), and using Eq. (32), a two-component reaction-diffusion system is obtained:

$$\sigma \frac{\partial u}{\partial t} = k_1' - k_2' u - \frac{4k_{3b}' uv}{h + u^2} + D_u \nabla^2 u \quad (33)$$

$$\frac{\partial v}{\partial t} = k_2' u - \frac{k_{3b}' uv}{h + u^2} + D_v \nabla^2 v, \quad (34)$$

where $k_1' = k_{1a}[\text{MA}]_o[\text{I}_2]_o/(k_{1b} + [\text{I}_2]_o)$, $k_2' = k_2[\text{ClO}_2]_o$, $k_{3b}' = k_{3b}[\text{I}_2]_o$, and $\sigma = 1 + K' > 1$. The subscript ‘‘o’’ refers to the concentrations of species which are taken to be constant, and u and v represent the concentrations of I^- and ClO_2^- species. The role of the immobile starch color indicator in providing the relative slowdown of the reaction and diffusion of the activator with respect to that of the inhibitor enters through the parameter $\sigma > 1$.

V. ANALYSIS

In this section, we use the LRE chemical model to investigate several aspects of the experimental CIMA system. The focus is to demonstrate the potential for quantitative analysis of experimental results using the realistic CDIMA chemical model. In Section V A, we investigate numerically the formation of one-dimensional multifront localized structures along the gradients of imposed boundary feeds. We study the linear stability of these structures to transverse symmetry-breaking perturbations using the two-variable reduction of the LRE model. We compare our results from a local analysis to that from a fully nonuniform analysis. We review a proposed modification to the local analysis and show that it does not successfully account for the presence of gradients. In Section V B, we further explore the structure and linear stability of the one-dimensional patterns along the boundary feeds as a function of two control parameters: the malonic acid reservoir concentration and gel width. We map out the linear instability intervals in each case. We discuss the qualitative agreement of our results with relevant experiments.

A. Linear Analysis of One-Dimensional Patterns Along Gradients

1. Stationary solution along the z -direction

The full 7-component LRE model equations given in Eqs. (25)–(31) were evolved forward in time to obtain the steady state solution in one dimension along the gradients. The boundary conditions, $[\text{MA}]_L = 1 \times 10^{-2}$ M at the left boundary, and $[\text{I}_2]_R = 1 \times 10^{-3}$ M and $[\text{ClO}_2]_R = 6 \times 10^{-4}$ M at the right boundary, were chosen so as to be consistent with a previous numerical investigation of the LRE model in one dimension by Lengyel *et al.* [19]. Since the boundary conditions giving a transverse instability were *a priori* unknown, we used these values as our starting point. The spatial z -direction was discretized on an irregularly spaced mesh to allow a greater number of mesh points in the regions where there was more structure in the solution, without excessively increasing the overall number of mesh points

in the problem. A five-point finite-difference approximation to the diffusion operator was used on the variable mesh. The numerical scheme employed for the time evolution was Crank-Nicholson implicit time-stepping for the linear terms, and Adams-Bashford explicit time-stepping for the nonlinear terms. A banded solver [22] was used at each time step to solve for the solution at the next time step. The initial concentrations were uniform in the z -direction (and equal to 5×10^{-13} M). The time evolution was continued until there was no appreciable change in the solution.

The results are displayed in Figure 2. The steady state solution for the starch-triiodide complex (SI_3^-) plotted in Figure 2(f) represents the experimentally observable profile. As expected, it tracks the iodide (I^-) steady state solution in Figure 2(d). It corresponds to a (non-symmetry breaking) pattern of stripes parallel to the feed boundaries (in the $x - z$ plane, with x being the uniform direction), such as those observed by Perraud *et al.* [15], although the boundary species are different in their experiments on the CIMA reaction from those considered here. Upon increasing the $[ClO_2^-]$ reservoir concentration, they observe a break-up of the stripes to rows of spots parallel to the feed surfaces. This is a symmetry-breaking instability, since the boundary feed symmetry of the system is broken. In the following, we will investigate the linear stability of our numerical steady state along the gradients to such a transverse pattern-forming instability.

2. Locally uniform stability analysis

To examine the stability of the stationary patterns that form along the gradients of boundary feeds (z -direction), the simplest approach is to treat each location z as being independent and locally uniform in the transverse plane (see Section II C), thereby neglecting diffusion along the z -direction (longitudinal diffusion). The locally homogeneous stationary state in the dynamical species, I^- and ClO_2^- , at each z can be constructed either from the linear (diffusion only) profiles of the reservoir species, MA, I_2 , and ClO_2 , or more correctly, from their reaction+diffusion profiles, obtained by evolving the full model, Eq. (25)–(31). In either case, using the two-variable activator-inhibitor reduction of the LRE model, Eqs. (33)–(34), the resulting eigenvalue problem for the stability of the locally homogeneous steady state to a symmetry-breaking instability requires a simple 2×2 analysis. Hence, it is desirable to use such a local approach if it can be shown that it accurately describes the physical problem. In that case, a transverse instability would occur in a region of width Δ along the gradients which is linearly unstable to a $k \neq 0$ instability. Indeed, even though Turing patterns are obtained under experimental conditions that by necessity lead to nonhomogeneous parameter ramps, a local linear analysis is most commonly used to predict the formation of a transverse symmetry-breaking instability. In this section, we examine in the context of the two-variable LRE model the locally uniform approach to determining the stability of the stationary patterns that form along the gradients of boundary feeds.

The locally uniform steady state in the variables I^- and ClO_2^- at each point in z along the gradients of the background chemicals is shown in Figure 3. This solution is obtained according to Eqs. (33)–(34) using the numerical reaction+diffusion profiles of Figure 2 for the MA, I_2 and ClO_2 species, but neglecting the diffusion terms. The dependence on z in this plot is parametric.

The stability of the local steady state at each z is obtained from Eq. (6). This analysis

predicts the existence of a finite instability region. The curves in Figure 4 represent the Turing instability condition boundaries, Eqs. (9)–(12), for each locally uniform steady state. We have also plotted the boundary which, when less than zero, gives the interval in z where the locally uniform steady state has a complex conjugate pair of eigenvalues for a range in k given by Eq. (A12). The vertical axis has no labels since we have plotted quantities which have different dimensions and only their signs are of interest. The shaded region denotes the interval over which the locally uniform steady state in the $x - y$ plane is linearly stable to homogeneous perturbations and unstable to inhomogeneous perturbations. The width Δ of this region is approximately 0.15 mm, which is within the 0.13 – 0.33 mm range of experimentally observed Turing wavelengths [23].

Figure 5 shows the gain curves for the locally uniform steady states at selected points along the z -axis, consistent with the above linear stability boundaries. Note that Figs. 5(d)–(i) illustrate the role of the complexing agent ($S + I_2$) in suppressing the oscillatory instability, since the concentration of I_2 (and therefore the complexing strength) sharply increases as the right boundary is approached.

3. Fully nonuniform stability analysis

To assess the validity of the locally uniform stability analysis presented above, we have carried out a fully nonuniform analysis, as described in Section II B. The eigenvalue problem given in Eq. (18) was discretized on the same variable mesh as that on which the nonuniform steady state was obtained, and was solved for all eigenvalues and eigenvectors at each value of transverse wave number k using EISPACK [24]. Since we have a general real matrix, with no special features such as symmetry, the most general routines were used. Figure 6 shows the real part of successive eigenvalues with largest real parts. This result shows the steady state to be stable to all transverse perturbations. The eigenvector with slowest decaying (real) growth rate at $k = 81.6 \text{ cm}^{-1}$ is plotted in Figure 7. It is localized roughly in the region along z where the locally uniform stability analysis predicts the corresponding uniform steady state to be unstable to a transverse instability.

Since we are generally interested in the most unstable mode, in this case, we checked the numerical validity of the gain curve for the slowest decaying eigenvector (top-most continuous curve in Figure 6) against two different numerical methods. First, the linear system for $2N_z$ variables (eigenvector), where N_z is the number of mesh points, was solved as a nonlinear root finding problem in $(2N_z + 1)$ variables, including the eigenvalue. Second, starting with the eigenvalue and eigenvector based on the previous two methods, inverse iteration was used to verify the results. Both checks agree with the results from EISPACK.

The convergence of the slowest decaying gain curve as a function of the variable mesh was also investigated. Starting with a particular distribution of mesh points, the mesh size was successively halved, the corresponding steady state obtained, and the eigenvalues and eigenvectors found. Basically, the number and distribution of mesh points must be sufficient to well resolve both the structure of the steady state and its most unstable eigenvectors for numerical convergence. All numerical calculations were performed on an IBM RS6000 workstation, with the exception of eigenvalue/eigenvector determination using EISPACK with greater than approximately 500 mesh points, which was done on a CRAY C90.

This result contradicts that from the locally uniform analysis which predicts a linear instability for these reaction parameters and boundary conditions. Below, we review a proposed modification to the locally uniform analysis, and determine whether it is sufficient to bring the local analysis closer to the fully nonuniform one.

In the above analysis and in those discussed in Section V A 2, we have used the two-variable reduction of the LRE model. We have directly verified the two-variable reduction of the full 7-variable (including H^+) model by performing a 7-variable linear stability analysis of the nonuniform stationary state using inverse iteration. By comparing the 7-variable and 2-variable linear stability results, we have implicitly verified the assumption that the reservoir species, MA, I_2 and ClO_2 , do not play a role in determining the pattern-forming instability of the stationary states [11].

4. Modified local stability analysis

The locally uniform analysis neglects diffusion along z which couples quasi-two-dimensional uniform slices. Lengyel, Kadar and Epstein (LKE) [16] have proposed a modification to account for this diffusion, assuming that diffusion along z is relevant only on a length scale of the order of the Turing wavelength. The basic idea behind the LKE modification is simple. In the presence of gradients in the z -direction, the Turing unstable mode is “split” between its “longitudinal” (along z) and “transverse” dependence:

$$k_c^2 = k_z^2 + k_\perp^2, \quad (35)$$

where k_c is the critical wave number in the (narrow) Turing unstable region along z , depending only on the local values of reaction and diffusion parameters. A transverse instability can occur provided the width of this region is not smaller than a Turing wavelength.

This modified local analysis is used to better predict the region along the gradients where a transverse instability occurs, and to obtain more accurately parameter values for investigating (transient) Turing patterns in batch reactors. The mechanics of the modification consists of adding an approximate term to the governing equations for the diffusion of the steady state along z , which does not alter the composition of locally uniform steady state but does affect its stability. This approximation to the diffusion operator is given by:

$$\frac{\partial^2 u}{\partial z^2} \approx \frac{u(z - \frac{\Delta}{2}) - 2u(z) + u(z + \frac{\Delta}{2})}{(\frac{\Delta}{2})^2} \approx \frac{8(\bar{u} - u(z))}{\Delta^2}, \quad (36)$$

\bar{u} is the average value of the locally uniform steady state on the two sides of the region of width Δ , which is characteristic of the longitudinal variation of the steady state. The validity of this estimate relies on the smallness of this width. The reaction terms f and g are modified:

$$f'(u, v; \vec{\mu}(z)) = f(u, v; \vec{\mu}(z)) + 8D_u((\bar{u} - u(z))/\Delta^2), \quad (37)$$

$$g'(u, v; \vec{\mu}(z)) = g(u, v; \vec{\mu}(z)) + 8D_v((\bar{v} - v(z))/\Delta^2), \quad (38)$$

and the Jacobian of the reaction terms, a_{ij} , in the linear stability analysis is modified accordingly. The Turing conditions can be rewritten as:

$$K'(z) > H_1(z) > H_2(z), \quad (39)$$

where

$$H_1 \equiv -a_{11}/a_{22} - 1, \quad (40)$$

$$H_2 \equiv -\frac{a_{11}}{2\sqrt{c(a_{11}a_{22} - a_{12}a_{21}) - ca_{11}}} - 1. \quad (41)$$

The range of the Turing instability is given by the crosspoints of K' and H_1 and of H_1 and H_2 . Since a_{ij} depend on Δ which is a priori unknown, H_1 and H_2 are evaluated iteratively from an initial estimate for Δ until convergence is achieved.

Figure 8 shows that the effect of this modification is to extend the z -range of the transverse instability from approximately one to two Turing wavelengths. The boundaries given by the functions $K'(z)$, $H_1(z)$ and $H_2(z)$ are combinations of the boundaries given in Figure 4 which resulted directly from the linear instability conditions. Therefore, although the representation of the boundaries in Figure 4 differs from that in Figure 8, the instability region is the same in the unmodified case.

The proposed modification increases the range of the Turing instability by suppressing the homogeneous oscillatory instability (moving the left boundary to the left), while not affecting the right boundary corresponding to the inhomogeneous instability. Identifying the left boundary of the z -range in which transverse patterns would form with the homogeneous instability is unphysical, since there is no mixing of modes at the linear level. Instead, it seems more appropriate to identify the left boundary of the Turing region with the z -location where an inhomogeneous instability ceases to exist ($ca_{11} + a_{22} = 0$).

An alternate modification to the local analysis is to carry out the linear stability analysis about the nonuniform steady state along z , such that the diffusion operator in the governing equations acts only on the steady state and not on the instability eigenvector in the z -direction. This ‘‘local’’ analysis incorporates the effect of diffusion along z through the nonuniform steady state, but the instability eigenvectors are ‘‘local’’ and depend only parametrically on z . The resulting eigenvalue problem becomes:

$$\begin{pmatrix} (a_{11}(z) - k^2)/\sigma & a_{12}(z)/\sigma \\ a_{21}(z) & a_{22}(z) - ck^2 \end{pmatrix} \begin{pmatrix} \delta u_k(z) \\ \delta v_k(z) \end{pmatrix} = \lambda_k(z) \begin{pmatrix} \delta u_k(z) \\ \delta v_k(z) \end{pmatrix}, \quad (42)$$

where $a_{ij}(z)$ are evaluated at the nonuniform steady state, and $(\delta u_k(z), \delta v_k(z))$ and $\lambda_k(z)$ depend parametrically on z . The stability boundaries are very irregular and not shown in this case. Except at the sharp edges of the nonuniform steady state and over a region roughly equal to the width of the sharp edge (much smaller than a Turing wavelength), this analysis predicts no $k \neq 0$ instability.

5. Discussion

We conclude that to accurately predict the formation and location of the Turing instability region, at least the one-dimensional steady state along the gradients must be solved for numerically using the full model including longitudinal diffusion. A ‘‘local’’ stability

analysis about this steady state does reproduce the result from the fully nonuniform stability analysis. However, a local analysis neglecting longitudinal diffusion of the stationary state does not correctly describe the linear stability of this state. We have presented here a first direct demonstration of this point by carrying out a fully nonuniform as well as a local linear stability analysis. As has been suggested [20], two-dimensional (nonlinear) time evolution of the model is the definitive method for predicting a transverse instability. We have accomplished this for the LRE model, and the results will be published elsewhere [29].

The locally uniform steady state profiles for the two dynamical variables I^- and ClO_2^- (Figure 3) do not include diffusion along the z direction and are qualitatively different from the numerical solution including diffusion (Figs. 2(d), (e)). Hence, it is not surprising that the local stability analysis about this steady state does not agree with the fully nonuniform one. In particular, at the left boundary, the locally uniform ClO_2^- profile is several orders of magnitude greater than the corresponding numerical solution including diffusion. This large discrepancy is accounted for by the diffusion of this species in a region extending over approximately the left half of the gel, as can be seen from the almost linear (diffusive) profile for ClO_2^- over this region (Figure 2(e)). The LKE modification to the locally uniform analysis, which corrects for this diffusion of the steady state along z , assumes that it is relevant only on the length scale of the order of the Turing wavelength. For the parameter values investigated here, this assumption is not valid, and the modified stability analysis does not correctly predict the stability of the structures along the gradients.

The dependence of the locally uniform steady state profiles for the intermediate species on the background concentration gradients is through the reaction terms. The results presented here are for background profiles obtained from reaction and diffusion of all six species. We have checked that these background stationary profiles do not vary considerably from those obtained by setting the intermediate species identically equal to zero. In this way, we rule out the possibility that the diffusion of the intermediate species feeds back into the profiles of the background variables, thereby accounting for the large discrepancy between the locally uniform steady state profiles of the intermediate species and those including diffusion. In particular, the large left boundary value of the locally uniform ClO_2^- species results from the strong suppression of I_2 relative to ClO_2 at this boundary, which becomes even more pronounced with backgrounds obtained from the intermediate species set identically equal to zero.

It is desirable to obtain semi-analytical solutions to the stationary structures along the gradients, which could then be used in (semi-analytical) linear stability analyses of these states. This has been done, for example, for the Brusselator model in the presence of slow spatial gradients using a WKB-like approach [25,26]. The localized structures along the gradients are obtained as marginally stable perturbations to the locally uniform steady state. However, in the case presented here, it is not possible to carry out a similar analysis. First, there is a large discrepancy at the boundaries between the locally uniform solution and the desired solution including diffusion satisfying Dirichlet boundary conditions. Even if the boundaries are ignored and an approximate solution in the interior of the gel is sought, our numerical results show that the steady state including diffusion is not a weakly nonlinear perturbation to the locally uniform steady state. Therefore, seeking a correction given by marginally unstable modes is not justified. For small gel width (see Sec. VB 2), where the background concentration profiles are almost linear, such a WKB-like description relying on

the slowness of the parameter ramps can perhaps be sought.

Numerical calculations based on the two-variable LRE model with uniform background have shown the transition to a symmetry-breaking instability to be strongly subcritical [27,28]. Although it is not clear how the range of parameters investigated in these works compares with their local values in the actual ramped experimental system or in our numerical example, these results imply that a *linear* stability analysis of the locally homogeneous steady states would not predict the existence of a finite amplitude instability in the subcritical regime. The nature of the transition of the fully nonuniform stationary structures along the ramps to a transverse symmetry-breaking instability has not been determined yet. Should this transition be supercritical, or even weakly subcritical, the fully nonuniform linear stability analysis would well predict the formation of quasi-one-dimensional symmetry-breaking spots in the thin-strip experiments. This is currently under investigation [29].

B. Parameter Dependence of the Turing Instability in the CDIMA System

As discussed in the previous section, by adopting a locally-uniform approach, existing numerical studies of the stability of the stationary patterns along feed gradients have not fully taken into account the reaction+diffusion feed gradients. Thus, the parameter range for the occurrence of a transverse symmetry-breaking instability in a gradient system within the context of the LRE model is essentially unknown. Hence, we have undertaken a systematic search, using the concentration of one of the reservoir species and the gel width as the control parameters. Variation of either of the control parameters changes the nonlinear reaction+diffusion profile of the background species, however they are not equivalent operations. In the following sections, we present our numerical results and make connection with relevant experimental work.

1. Variable malonic acid boundary condition

The parameter search for the Turing instability in the CDIMA reaction-diffusion system as a function of the malonic acid concentration at the left boundary was performed for $[MA]_L$ in the range 0.004 M to 0.035 M. The concentrations $[I_2]_R$ and $[ClO_2]_R$ at the right boundary were held fixed at 0.008 M and 0.006 M, respectively. These values were chosen so as to lie within the range of the initial concentrations of these species used in experiments on this system in batch reactors [17], and therefore should also be experimentally accessible in open reactors.

First, we numerically obtained steady state solutions of the full 7-variable governing equations as a function of $[MA]_L$, as described in Section V A 1. The analysis described in Section V A 3 of the linear stability along the gradients to transverse symmetry-breaking perturbations was repeated for each stationary state. This was performed using the reduction of the full LRE model to the two dynamical variables I^- and ClO_2^- . The eigenvalue and eigenvector corresponding to the fastest growing (or slowest decaying) mode at each value of the transverse wave number k were obtained numerically using inverse iteration, and confirmed for select values of k using EISPACK [24].

In Figure 9, we have plotted the value of the control parameter $[MA]_L$ versus wave number, with the solid boundaries denoting marginally stable wave numbers. The shading indicates the Turing-unstable regions. We note that the unstable regions are disjoint, corresponding to the following scenario: as the control parameter is continuously varied, the stable stationary state along the gradients first becomes unstable to transverse Turing patterns at a critical value of the control parameter, and initially remains unstable as the control parameter continues to increase. It becomes stable again once the control parameter exceeds a second and higher critical value. This is qualitatively consistent with the experimental observations of Perraud *et al.* [15] on the CIMA reaction-diffusion system. Their results show that as the concentration of $[ClO_2^-]_R$ at the right boundary is increased, the number of alternating dark and bright bands parallel to the feed boundaries increases, and several layers break up into rows of spots. As $[ClO_2^-]_R$ continues to be increased, the spot patterns develop along more bright bands, until they eventually disappear and the parallel stripes are recovered.

In Figure 10, we have plotted the stationary solutions for the experimentally observed SI_3^- species from our numerical calculation, at various values of $[MA]_L$. We observe that the number of peaks in the steady state solution increases with increasing $[MA]_L$, while the characteristic “wavelength” of the patterns along the gradients remains relatively constant (excluding the leftmost peak). The transition from one unstable region to another corresponds roughly to the appearance of an additional peak in the stationary solution along the gradient: instability region I corresponds to a steady state with three peaks, region II corresponds to four peaks, and region III corresponds to five peaks. As an example, for the instability region II, we show in Figure 11 density plots of the steady state and the fastest growing (slowest decaying) wave vector. This eigenvector is localized at and roughly tracks one of the minima in the steady state solution. This is also the case for regions I and III. Specifically, the unstable vector appears to be approximately localized at the next-to-last minimum of the SI_3^- solution. The appearance of the symmetry-breaking instability at a minimum of the starch-triiodide is consistent with the above experimental observations.

To better quantify this trend, in Figure 12, we plot the value of all six chemical species at successive minima of the SI_3^- stationary solution as a function of $[MA]_L$. In this figure, the circles, triangles, squares and diamonds correspond to the second, third, fourth and fifth minima, respectively. The points corresponding to critical $[MA]_L$ values are filled (two points for each unstable region). We note that the relevant chemical species for tracking the instability are the two dynamical species, I^- and ClO_2^- , plotted in Figure 12(d) and (e). (The SI_3^- concentration depends on the product of the I^- and I_2 concentrations.) The concentration of I^- remains within the range of approximately $(1.0 - 2.2) \times 10^{-7} M$, and the concentration of ClO_2^- remains approximately constant at 1×10^{-6} in each of the instability regions. (Note that the concentration of SI_3^- does not stay within a more-or-less constant range for each of the instability regions due to the drift in the I_2 concentration.) A simple interpretation of these numerical results is that an instability occurs when the concentrations of the dynamical species I^- and ClO_2^- lie within a certain range. As the stationary solution changes with increasing $[MA]_L$, the instability vanishes when the value of the concentration of the steady state falls outside of this range, and reappears when the concentration at the *next* minimum is within this range again.

The experiments of Perraud *et al.* [15] show that as the control parameter is increased,

the stationary pattern of stripes along the gradients first becomes unstable in a single stripe region and then in multiple stripes as the control parameter continues to increase. In our numerical investigations, the most unstable vector remains singly peaked in all cases. To further investigate this point, we have examined the spatial structure (along z) of the linear instability eigenvectors as a function of k . Figure 13 shows a density plot of the most unstable (or least stable) eigenvector, corresponding to the I^- species, as a function of transverse wave number k for $[MA]_L = 0.023$ M. The horizontal axis represents the spatial coordinate along the gradients, and the vertical axis is the transverse wave number, ranging from $k = 0$ cm^{-1} to $k = 900$ cm^{-1} .

In Figure 14, we show the first fourteen eigenvalues with largest real parts as a function of k . We note the eigenvalue crossings that define distinct “modes” cutting across the spectrum of eigenvalues. As an interesting aside, we have investigated the eigenvectors corresponding to one such “mode”, denoted by filled triangles in this figure. The spatial profile of these eigenvectors changes continuously with increasing k . Hence, their interpretation as a single physical “mode” is not obvious. There does not appear to be a mode crossing between the first and second branches of Figure 14, although the structure of the first eigenvector changes considerably from being multi-peaked (and stable) to being singly peaked (and unstable, but subsequently stable again) as k increases. The experiments of Perraud *et al.* could correspond to a case where, as the control parameter is varied, a mode with multiple peaks becomes unstable. This does not occur in our numerical investigation, where the multiply peaked modes remain stable. The appearance of multiple instability layers could also be a nonlinear effect, resulting from linear growth and nonlinear saturation of the singly peaked unstable eigenvector, as well as growth of its side lobes. However, we have shown [29] that in the two-dimensional evolution of the governing equations, the spatial profile of the most linearly unstable mode is in fact preserved in the LRE model.

2. Variable reservoir length along boundary feeds

The experiments of Dulos *et al.* [14] have aimed at elucidating the transition from quasi-two-dimensional to three-dimensional Turing patterns by combining observations in bevelled thin-strip and disc reactors. Motivated by these experiments, we have undertaken a similar numerical investigation which does not directly address the same question, but rather continues to focus on the localized patterns along the ramps. In particular, we consider the experimental results from the variable-width thin-strip reactor. In these experiments, the transition between the domains with one and two rows of spots, and the possible influence of the feed gradients on the phase relations between the spots in the two rows have been studied. The vanishing amplitude of the spot modulations before this splitting occurs is not well understood.

Our numerical results address the latter question. We have reproduced the observed qualitative trend of the symmetry-breaking instability occurring and subsequently disappearing in a single layer as the gel width is varied. The boundary conditions are held fixed at $[MA]_L = 0.023$ M, $[I_2]_R = 0.008$ M and $[ClO_2]_R = 0.006$ M, while the gel width is varied from 0.14 – 0.39 cm. The stationary localized patterns along the gradients as a function of the scaled gel width are shown in Figure 15. Figure 16 shows the linear stability of each solution to a symmetry-breaking instability. In Figure 17, we have plotted the value of the

control parameter w versus wave number k , with the solid boundary denoting the marginally stable wave numbers. For the parameter values and boundary conditions numerically investigated here, we do not observe the transition from an unstable monolayer to an unstable bilayer as the gel width is increased. We have followed the most linearly unstable $k \neq 0$ mode as the gel width is varied, and it remains singly peaked.

These numerical results are analogous to those presented in Section VB 1, where the parameter dependence of the Turing instability in a ramped system was investigated as a function of the malonic acid boundary condition. Here also, we track the concentrations of the chemical species at the location of the minimum of the starch-triiodide complex where the fastest growing/slowest decaying instability eigenvector is localized. The results are given in Figure 18: as before, triangles, circles, squares, and diamonds represent the second, third, fourth and fifth minimum, respectively. The solid squares correspond to the critical lengths, below and above which the instability vanishes. We note the following about the concentrations of the chemical species in the unstable interval (at the third minimum of the stationary SI_3^- solution): (1) the concentration of ClO_2^- is approximately at 1×10^{-6} M, in agreement with the variable $[\text{MA}]_L$ investigation, (2) the concentration of I^- is in the approximate range of $1.8 - 2.2 \times 10^{-7}$ M, again in agreement with the variable $[\text{MA}]_L$ investigation, and (3) the concentrations of the background species, MA, I_2 and ClO_2 are approximately equal to those in the variable $[\text{MA}]_L$ case for region III of Figure 9. These results support the simple interpretation that the concentrations of the dynamical species, the activator I^- and the inhibitor ClO_2^- , are key factors in the occurrence of a transverse instability. However, this picture may be overly simplified: for values of gel width larger than the upper critical value, the concentrations of I^- and ClO_2^- remain well within the instability interval of the variable $[\text{MA}]_L$ analysis while the stationary state remains stable.

3. Discussion

In this section, we have explored the parameter dependence of the Turing instability as a function of malonic acid boundary condition and gel width. The use of the CIMA reaction-diffusion system (as opposed to the CDIMA system) and its corresponding boundary species (iodide, rather than iodine, and chlorite, rather than chlorine) by experimenters makes direct comparison of our numerics with their results difficult. Nevertheless, our numerical simulations display similar features to those present in experimental results as control parameters are varied. These are: (1) the transition to patterns with progressively larger numbers of fronts, and (2) the appearance and subsequent vanishing of a transverse instability. Also agreeing with experimental results, the instability is localized near a minimum of the starch triiodide (as well as iodide) unperturbed solution. For the parameters and boundary conditions we considered in our numerical investigations, the multiply-peaked linear instability eigenvectors remain stable, and the experimentally observed transition from a single to multiple unstable layers is not obtained. Overall, the agreement between trends in these experiments and our numerics is encouraging, and will hopefully provide motivation for future experiments on the CDIMA system which could be compared quantitatively with numerical and analytical results.

VI. CONCLUSIONS

In this work, we have focused on the one-dimensional patterns that form in the presence of feed gradients, a necessary feature of the real experimental systems. We have shown that longitudinal diffusion along the boundary feed gradients can be important over length scales longer than the Turing wavelength. Therefore, the frequently-invoked locally uniform approach for predicting the linear instability of the stationary patterns along the gradients to a transverse symmetry-breaking instability is inappropriate in such cases.

We have also explored the dependence of the Turing instability of these longitudinal structures on two control parameters. The transition to patterns with progressively larger number of longitudinal fronts and the appearance and subsequent vanishing of the transverse instability near a local minimum of the starch triiodide solution are features which are in agreement with experimental results. We have attempted to interpret these trends, by determining that a transverse instability occurs and is localized at that part of the stationary solution along the gradients where the values of the concentrations of the dynamical iodide and chlorite species are within a certain well-defined range. For the parameters and boundary conditions investigated here, we do not obtain the experimentally observed transition from a single to multiple Turing unstable layers.

Building on the work presented here, one can begin to address many interesting questions. At the linear level, it is clear from the numerical solutions that both the formation of localized structures along the gradients as well as their transverse instability are governed by the Turing mechanism. The relationship between the “longitudinal” and “transverse” pattern formation is an interesting question that so far has only been analyzed for model systems [30]. For the realistic chemical description it may be more feasible to address this question analytically in the limit where the reservoir concentrations can be approximated by linear profiles: we have found that these conditions are achieved, for parameter values explored in the variable gel-width numerical investigation, for small gel widths. A description of the longitudinal structures can perhaps be sought, in terms of wave number selection in the presence of control parameter ramps [31]. The effect of the variation in background concentration profiles, with changing gel width or malonic acid reservoir concentration (Figures 10 and 15), on these one-dimensional structures can be investigated within this framework. Alternatively the symmetry breaking transition might be better understood in terms of a fully three dimensional periodic instability perturbed by longitudinal gradients.

At the nonlinear level, the nature of the transition from one-dimensional non-symmetry breaking front patterns to symmetry-breaking transverse spots in thin-strip reactors (continuous or discontinuous) can be determined numerically from the nonlinear evolution of the LRE model in two dimensions [29]. Numerical establishment of the bifurcation behavior for the two-dimensional “monolayers” in disc reactors is also a relevant topic for further investigation, and would require extending numerical computation to three dimensions. Dufiet *et al.* [32] have pointed out that these monolayers which are confined by a transverse parameter ramp must be distinguished from what they call *genuine* two-dimensional structures which form under uniform control parameters. They have compared pattern selection in genuine two-dimensional systems and in such monolayers in the context of an abstract reaction-diffusion model. The advantage of using the LRE model is that results would then be directly comparable with experiments based on the CDIMA reaction. An interesting

feature of the work of Dufiet *et al.* is the coupling of the pattern forming modes to the longitudinal displacement of the pattern as a whole: it would be interesting to investigate this effect using the realistic description of the longitudinal gradients.

The successful formulation of a realistic model of the chlorine dioxide-iodine-malonic acid reaction-diffusion system has made this system an attractive paradigm for the study of nonequilibrium pattern formation [10]. This work represents an attempt at bringing theoretical and numerical study of pattern formation in chemical systems closer to experimental studies.

ACKNOWLEDGMENTS

This work was supported by the National Science Foundation under Grant No. DMR-9311444, and by a generous award of computer time from the San Diego Supercomputer Center. We thank Dan Meiron for useful advice on the numerics.

APPENDIX A: DETAILS OF THE TURING INSTABILITY CONDITIONS

1. Stability to Homogeneous Perturbations: $k = 0$

The characteristic equation for $k = 0$ is:

$$\sigma\lambda_o^2 - (a_{11} + \sigma a_{22})\lambda_o + (a_{22}a_{11} - a_{12}a_{21}) = 0, \quad (\text{A1})$$

with,

$$\lambda_o^{(\pm)} = \frac{1}{2\sigma}(a_{11} + \sigma a_{22}) \pm \frac{1}{2\sigma}\sqrt{(a_{11} + \sigma a_{22})^2 - 4\sigma(a_{11}a_{22} - a_{12}a_{21})}. \quad (\text{A2})$$

We require $\text{Re}(\lambda_o^{(\pm)}) < 0$. Therefore, in the case of $\text{Im}(\lambda_o^{(\pm)}) \neq 0$, we must have:

$$\lambda_o^{(+)} + \lambda_o^{(-)} = a_{11} + \sigma a_{22} < 0, \quad (\text{A3})$$

and additionally, in the case of $\text{Im}(\lambda_o^{(\pm)}) = 0$:

$$\lambda_o^{(+)}\lambda_o^{(-)} = \sigma [a_{11}a_{22} - a_{12}a_{21}] > 0. \quad (\text{A4})$$

2. Instability to Inhomogeneous Perturbations: $k \neq 0$

We require that at least one of the roots be positive for some $k \neq 0$. Consider the sum of the eigenvalues:

$$\lambda_k^{(+)} + \lambda_k^{(-)} = -(\sigma c + 1)k^2 + (a_{11} + \sigma a_{22}). \quad (\text{A5})$$

Once stability to $k = 0$ perturbations is imposed according to Eq. (A3), the above sum will be < 0 , and the real part of one of the roots is necessarily negative. First, we require that the product of the roots be < 0 in order to have a positive real root:

$$\lambda_k^{(+)}\lambda_k^{(-)} = \sigma \left(ck^4 - (a_{22} + ca_{11})k^2 + (a_{11}a_{22} - a_{12}a_{21}) \right) \equiv h(k^2) < 0. \quad (\text{A6})$$

Since the first and third terms in $h(k^2)$ are > 0 , a necessary condition for $h(k^2) < 0$ is:

$$a_{22} + ca_{11} > 0. \quad (\text{A7})$$

Furthermore, we know that $h(k^2)$ has a minimum, and from Eq. (A4) that:

$$h(0) = \sigma(a_{11}a_{22} - a_{12}a_{21}) > 0. \quad (\text{A8})$$

So, for $h(k^2) < 0$, k^2 must lie between the two roots k_-^2 and k_+^2 :

$$k_{\pm}^2 = \frac{1}{2c} \left[(a_{22} + ca_{11}) \pm \sqrt{(a_{22} + ca_{11})^2 - 4c(a_{11}a_{22} - a_{12}a_{21})} \right]. \quad (\text{A9})$$

For k_{\pm}^2 to be real, we must have:

$$(a_{22} + ca_{11})^2 - 4c(a_{11}a_{22} - a_{12}a_{21}) \geq 0. \quad (\text{A10})$$

Eq. (A10) is required for real values k_{\pm}^2 of the marginal modes, and Eq. (A7) is required for $k_{\pm}^2 \geq 0$. Equations (A3), (A4), (A7) and (A10) constitute the Turing conditions.

3. Oscillatory Instability

From Eq. (7) there will be a complex conjugate pair of eigenvalues, $\text{Im}(\lambda_k) \neq 0$, for:

$$g(k^2) \equiv (\sigma c - 1)^2 k^4 + 2k^2(\sigma c - 1)(a_{11} - \sigma a_{22}) + (a_{11} - \sigma a_{22})^2 + 4\sigma a_{12}a_{21} \leq 0. \quad (\text{A11})$$

To determine the behavior of $g(k^2)$, look at its roots:

$$k_{\pm}^{(\text{H})2} = -\frac{(a_{11} - \sigma a_{22})}{\sigma c - 1} \pm \frac{\sqrt{-4\sigma a_{12}a_{21}}}{\sigma c - 1}. \quad (\text{A12})$$

For $\text{Im}(\lambda_k) \neq 0$, require $k_+^{(\text{H})2} \geq 0$. Under typical experimental conditions, we expect $\sigma c - 1 > 0$. We note that $g(k^2)$ possesses a minimum with:

$$g(0) = (a_{11} - \sigma a_{22})^2 + 4\sigma a_{12}a_{21}. \quad (\text{A13})$$

Therefore, for $k_+^{(\text{H})2} \geq 0$, we must have $g(0) < 0$, in which case $\text{Im} \lambda_k \neq 0$ for $0 < k^2 < k_+^{(\text{H})2}$. The real part of the complex conjugate pair is given by:

$$\text{Re} \lambda_k = -\frac{1}{2} \left[(\sigma c + 1)k^2 - (a_{11} + \sigma a_{22}) \right], \quad (\text{A14})$$

and behaves as:

$$i) a_{11} + \sigma a_{22} < 0 \quad \Rightarrow \quad \text{Re} \lambda_k < 0 \quad (\text{A15})$$

$$ii) a_{11} + \sigma a_{22} > 0 \quad \Rightarrow \quad \text{Re} \lambda_k < 0 \quad \text{for} \quad k_+^{(\text{H})2} > k^2 > \frac{a_{11} + \sigma a_{22}}{\sigma c + 1} \quad (\text{A16})$$

$$\text{Re} \lambda_k \geq 0 \quad \text{for} \quad 0 < k^2 \leq \frac{a_{11} + \sigma a_{22}}{\sigma c + 1}. \quad (\text{A17})$$

REFERENCES

- [1] M. C. Cross and P. C. Hohenberg, *Rev. Mod. Phys.* **65**, 854 (1993).
- [2] Q. Ouyang and H. L. Swinney, *Chemical Waves and Patterns*, edited by R. Kapral and K. Showalter (Klewer, 1995), p. 269.
- [3] Turing, A.M., *Phil. Trans. R. Soc. London, Ser. B* **327**, 37 (1952).
- [4] V. Castets, E. Dulos, J. Boissonade, and P. De Kepper, *Phys. Rev. Lett.* **64**, 2953 (1990).
- [5] P. De Kepper, V. Castets, E. Dulos, and J. Boissonade, *Physica D* **49**, 161 (1991).
- [6] Q. Ouyang and H. L. Swinney, *Nature* **352**, 610 (1991).
- [7] J. D. Murray, *Mathematical Biology*, (Springer-Verlag, Berlin, 1989), Chp. 15.
- [8] I. Lengyel, G. Rabai, and I. R. Epstein, *J. Am. Chem. Soc.* **112**, 4606 (1990).
- [9] I. Lengyel, G. Rabai, and I. R. Epstein, *J. Am. Chem. Soc.* **112**, 9104 (1990).
- [10] G. Dewel, P. Borckmans, A. De Wit, B. Rudovics, J. J. Perraud, E. Dulos, J. Boissonade, and P. De Kepper, *Physica A*, **213**, 181 (1995).
- [11] S. Setayeshgar, *Turing Pattern Formation in the Chlorine Dioxide-Iodine-Malonic Acid Reaction-Diffusion System*, Ph.D. Thesis, California Institute of Technology, 1998.
- [12] J. E. Pearson and W. J. Bruno, *Chaos* **2**, 513 (1992).
- [13] Q. Ouyang and H. L. Swinney, *Chaos* **1**, 411 (1991).
- [14] E. Dulos, P. Davies, B. Rudovics, and P. De Kepper, *Physica D*, **98**, 53 (1996).
- [15] J. J. Perraud, K. Agladze, E. Dulos, and P. De Kepper, *Physica A* **188**, 1 (1992).
- [16] I. Lengyel, S. Kadar, and I. R. Epstein, *Phys. Rev. Lett.* **69**, 2729 (1992).
- [17] S. Kadar, I. Lengyel, and I. R. Epstein, *J. Phys. Chem.* **99**, 4504 (1995).
- [18] I. Lengyel and I. R. Epstein, *Proc. Natl. Acad. Sci.* **89**, 3977 (1992).
- [19] I. Lengyel and I. R. Epstein, *Science* **251**, 650 (1991).
- [20] I. Lengyel and I. R. Epstein, *Chemical Waves and Patterns*, edited by R. Kapral and K. Showalter (Klewer, 1995), p. 297.
- [21] I. Lengyel, S. Kadar, and I. R. Epstein, *Science* **259**, 493 (1993).
- [22] W. H. Press, S. A. Teukolsky, W. T. Vetterling, and B. P. Flannery, *Numerical Recipes in C* (Cambridge Univ. Press, 1992).
- [23] Q. Ouyang and H. L. Swinney, *Chaos* **1** (4), 411 (1991).
- [24] B. T. Smith, J. M. Boyle, J. J. Dongarra, B. S. Garbow, Y. Ikebe, V. C. Klema, and C. B. Moler, *Matrix Eigensystem Routines – EISPACK Guide* (Springer-Verlag, Berlin, 1976).
- [25] J. F. Auchmuty, and G. Nicolis, *Bulletin of Mathematical Biology* **37**, 323 (1975).
- [26] G. Dewel and P. Borckmans, *Physics Letters A* **138** (4), 189 (1989).
- [27] O. Jensen, V. O. Pannbacker, G. Dewel, and P. Borckmans, *Physics Letters A* **179**, 91 (1993).
- [28] O. Jensen, V. O. Pannbacker, E. Mosekilde, G. Dewel, and P. Borckmans, *Phys. Rev. E* **50**, 736 (1993).
- [29] S. Setayeshgar and M. C. Cross, article in preparation.
- [30] G. Dewel, D. Walgraef, and P. Borckmans, *J. Chim. Phys. (France)* **84**, 1335 (1987).
- [31] L. Kramer, E. Benjacob, H. Brand, and M. C. Cross, *Phys. Rev. Lett.* **49**, 1891 (1982).
- [32] V. Dufiet and J. Boissonade, *Phys. Rev. E.*, **53**, 4883 (1996).

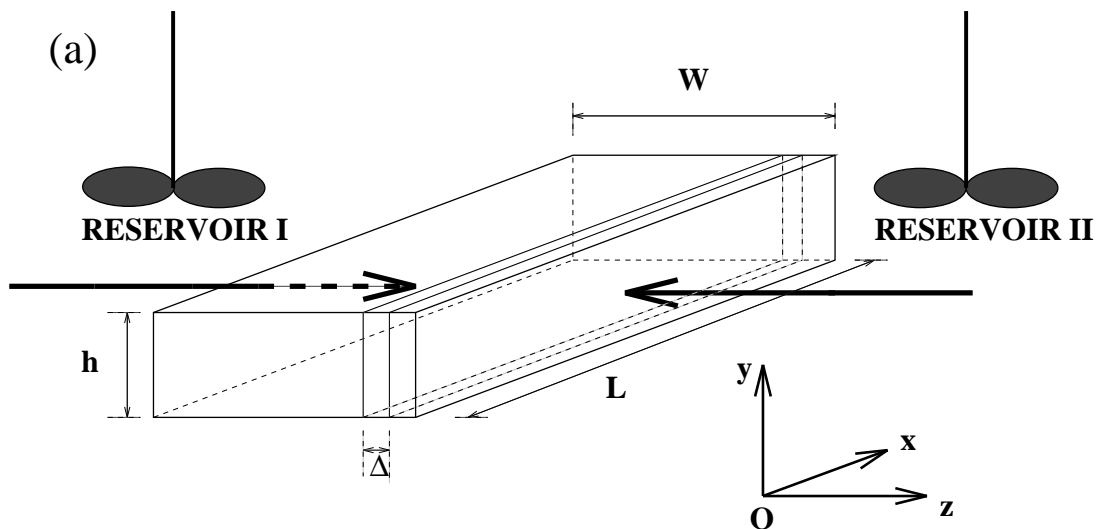


FIG. 1. Sketch of open reactor geometries, adapted from Refs. [10,14]: A block of gel, with dimensions $L \gg w > h$ is in contact with two reservoirs I and II. The reservoirs are continuously stirred and fed with fresh supplies of reactants, such that each is separately nonreactive. A gradient in the reservoir species forms perpendicular to the feed boundaries in the z -direction. The symmetry-breaking patterns form transverse to this gradient. The thickness Δ of the finite region along z where they form is equal to at least one wavelength λ of the Turing patterns.

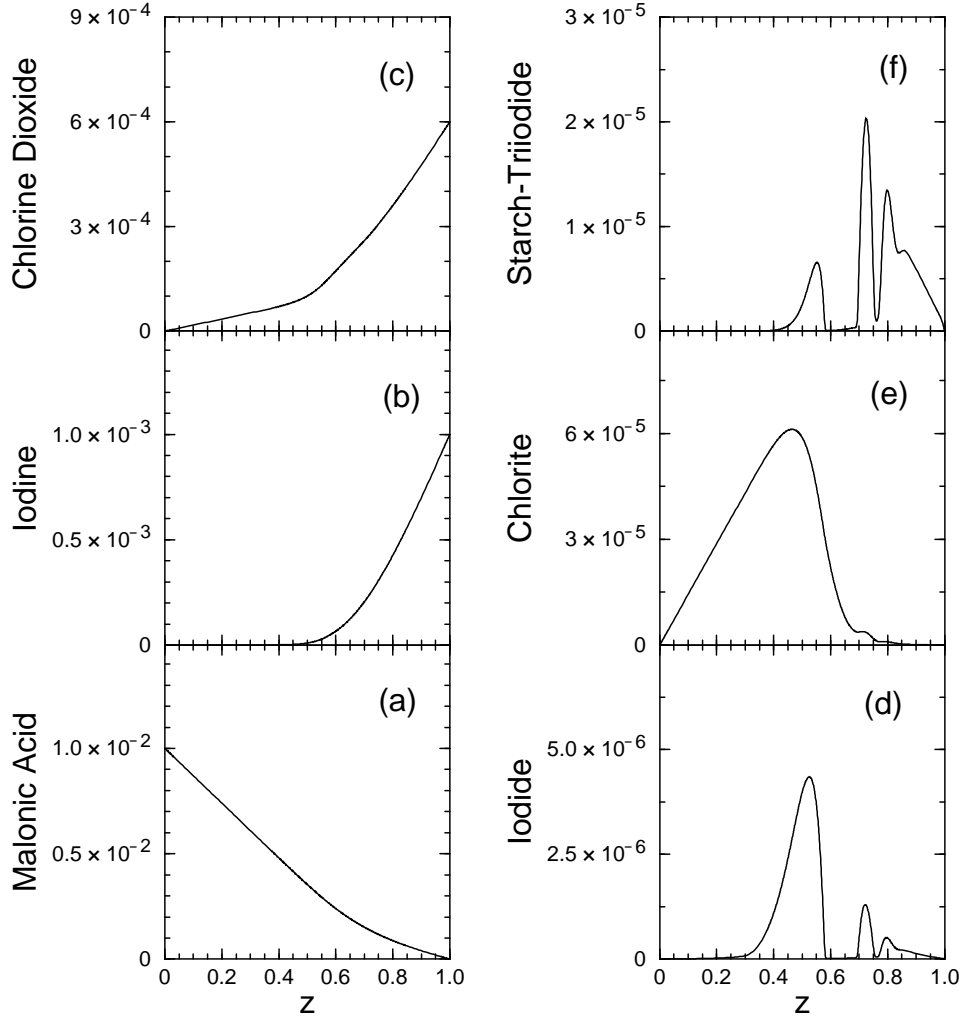


FIG. 2. One-dimensional steady state solutions: The boundary conditions are $[\text{MA}]_L = 1 \times 10^{-2}$ M at the left boundary, and $[\text{I}_2]_R = 1 \times 10^{-3}$ M and $[\text{ClO}_2]_R = 6 \times 10^{-4}$ M at the right boundary. All other boundary conditions are zero. The z -axis has been normalized with respect to the thickness of the gel in the z -direction, $w = 0.3$ cm. We note that the steady state profiles for the reservoir variables malonic acid (MA), iodine (I_2) and chlorine dioxide (ClO_2) vary considerably from diffusion-only linear profiles. The series of peaks in the starch triiodide (SI_3^-) profile correspond to experimentally observed stripes parallel to the feed boundaries [15].

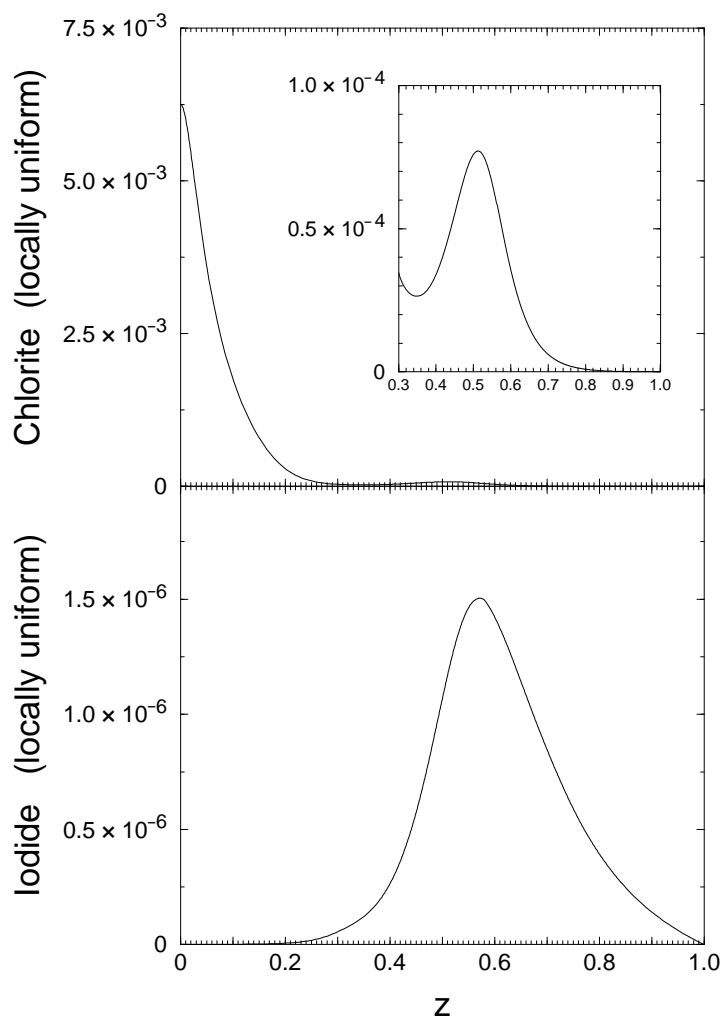


FIG. 3. The value of the steady state solution, locally uniform in the $x - y$ plane, is plotted at each point z for the two dynamical variables iodide (I^-) and chlorite (ClO_2^-) using the reaction + diffusion profiles of the reservoir variables given in Figure 2.

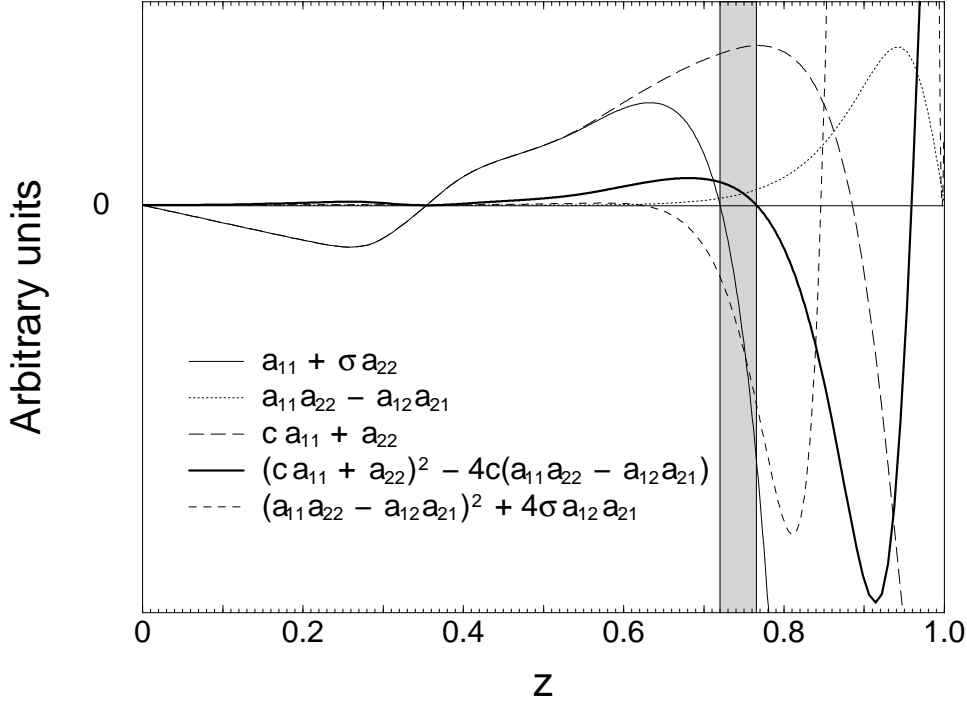


FIG. 4. Boundaries from locally uniform stability analysis: At each location z , the Turing instability conditions have been plotted for the corresponding uniform steady state. The plotted quantities have different dimensions, and since only the sign of each quantity is of interest, the vertical axis has no scale. When the light solid line corresponding to $(a_{11} + \sigma a_{22})$ is less than zero, the complex conjugate pair of eigenvalues for $k = 0$ has a negative real part. The dotted line is $(a_{11}a_{22} - a_{12}a_{21})$ which is additionally required to be greater than zero for stability of a real $k = 0$ mode. We note that this quantity is everywhere greater than zero. The long-dashed line corresponds to $(ca_{11} + a_{22})$, and the heavy solid line is $(ca_{11} + a_{22})^2 - 4c(a_{11}a_{22} - a_{12}a_{21})$, both of which must be greater than zero in order to have a $k \neq 0$ instability. The dashed line is $((a_{11} - \sigma a_{22})^2 + 4\sigma a_{12}a_{21})$, and where it is less than zero, a complex conjugate pair of eigenvalues exists for a finite range in k . The shaded region indicates where the locally uniform steady state is stable to homogeneous perturbations and unstable to inhomogeneous perturbations. At $z = 0.354$, the light solid $(a_{11} + \sigma a_{22})$ and long-dashed $(ca_{11} + a_{22})$ lines go through zero, while the heavy solid, dotted and dashed lines remain positive.

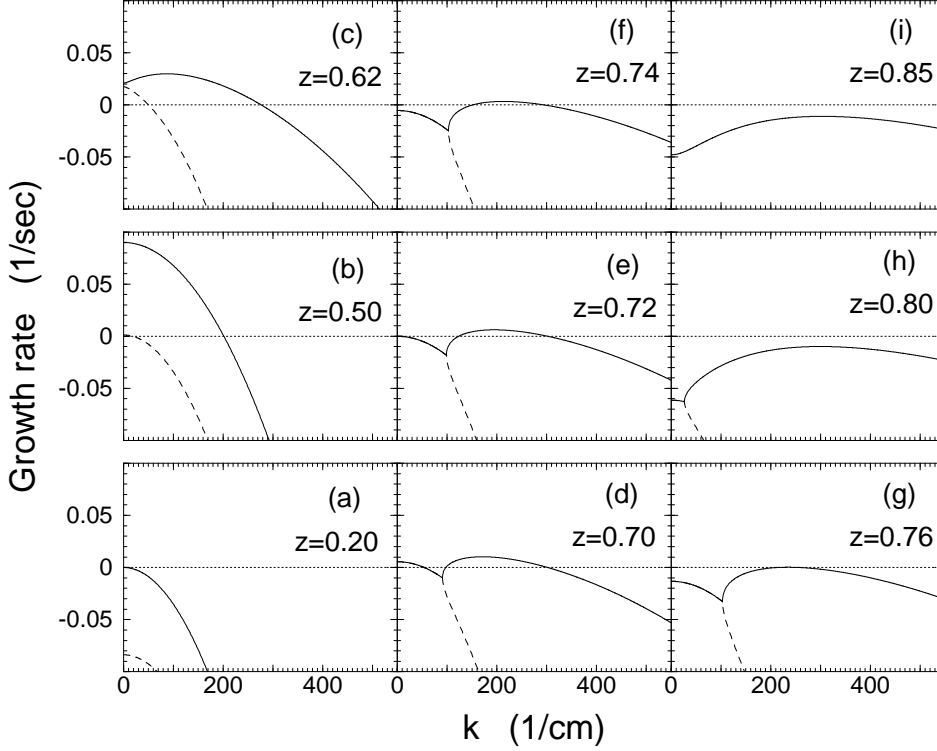


FIG. 5. Gain curves for locally uniform steady states: The solid line denotes the eigenvalue with the larger real part, λ_+ , and the dashed line denotes the one with the smaller real part, λ_- . At (a) $z = 0.20$, both eigenvalues are real and negative for all k ; (b) $z = 0.50$, both eigenvalues are real and peaked at $k = 0$, with $\lambda_+ > 0$ in the range $0 < k^2 < k_+^2$ and $\lambda_- > 0$ in the range $0 < k^2 < k_-^2$ (k_{\pm}^2 are given in Appendix A); (c) $z = 0.62$, both eigenvalues are still real, but at $k = 0$, we have a real degenerate pair, giving the boundary of the Hopf bifurcation; (d) $z = 0.70$, complex conjugate pair of eigenvalues with positive real part for $0 < k^2 < (a_{11} + \sigma a_{22})/(\sigma D_v + D_u)$, and $k \neq 0$ instability for $k_-^2 < k^2 < k_+^2$; (e) $z = 0.72$, same as (d), except that the real part of the complex conjugate pair is peaked at zero growth rate; (f) $z = 0.74$, same as (d) with the real part of the complex conjugate pair less than zero at $k = 0$; (g) $z = 0.76$, same as (f), except that the maximum growth rate for $k \neq 0$ is zero; (h) $z = 0.80$, same as (g), except that the maximum growth rate for $k \neq 0$ is negative; (i) $z = 0.85$, both eigenvalues are real and negative.

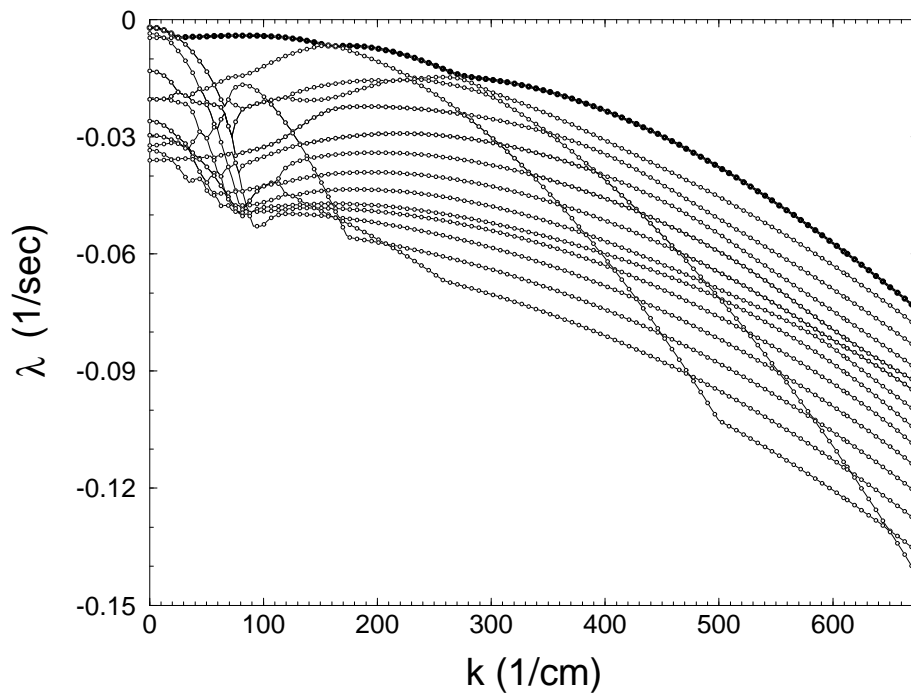


FIG. 6. Gain curve for the one-dimensional steady state along the gradients: The real parts of the first fourteen eigenvalues with largest real parts have been plotted. The eigenvalues are real, except at points (or along intervals) where two curves intersect. The eigenvalue crossings appear imperfect due to the coarse selection of k values. All eigenvalues are less than zero, with the heavy line corresponding to the slowest decaying mode at each k .

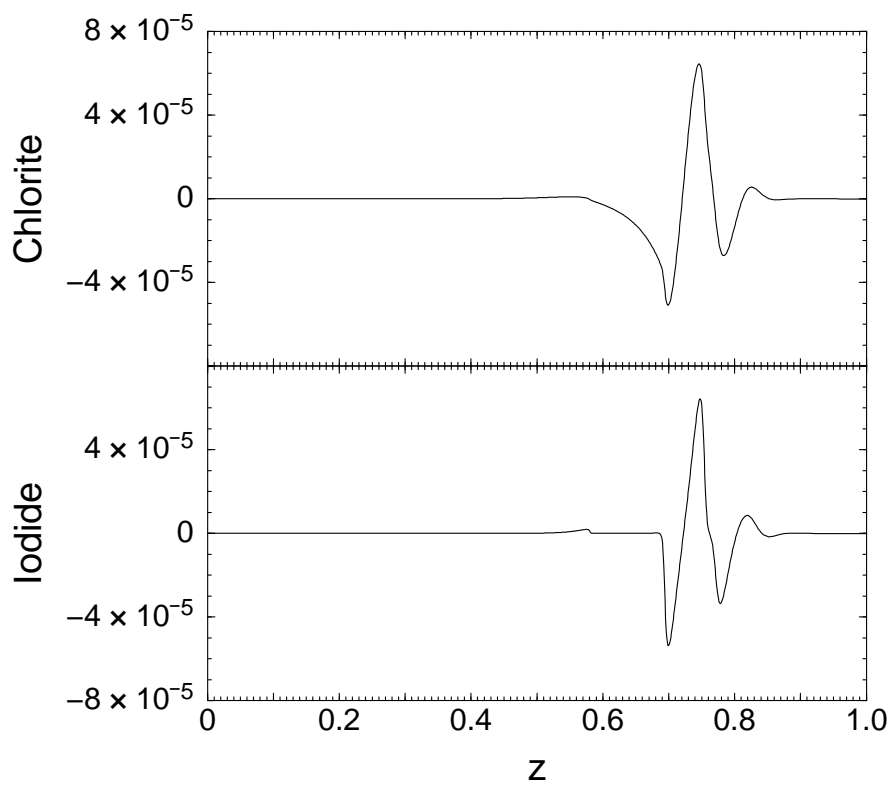


FIG. 7. Eigenvector corresponding to slowest decaying mode in a fully nonuniform analysis: The eigenvector at $k = 81.6 \text{ cm}^{-1}$ with the largest real eigenvalue has been plotted.

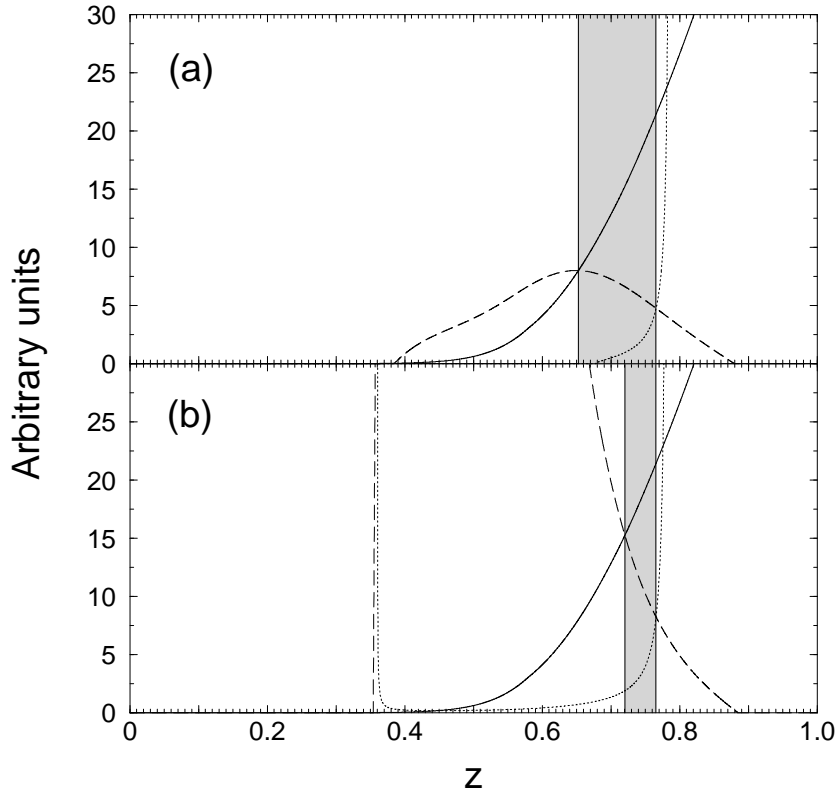


FIG. 8. Modified local stability analysis: K' , H_1 and H_2 are given by the solid, long-dashed and dotted lines respectively. In (a), these boundaries have been modified to take into account diffusion of the steady state along z , whereas in (b) they are unchanged. The Turing instability region is indicated by the shading. The shaded region in (b) is identical to that in Figure 4. Note that the right boundary of the Turing region, which denotes $k \neq 0$ criticality, remains unchanged under the modification.

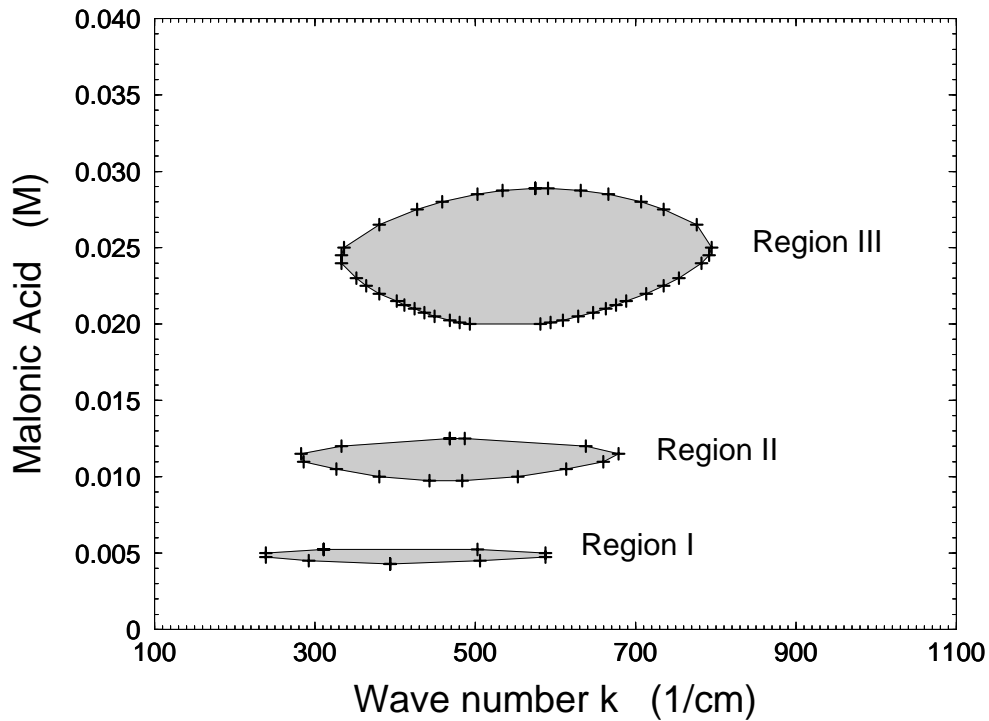


FIG. 9. Malonic acid concentration (M) at the left boundary versus the wave number k of the transverse instability (1/cm): The crosses represent the marginally stable wave numbers determined from the stability analysis of the one-dimensional steady states corresponding to the given malonic acid feed concentration. A transverse instability occurs for values of malonic acid feed concentration in the shaded regions, with the range of linearly unstable modes delimited by the solid lines for each value of $[\text{MA}]_L$.

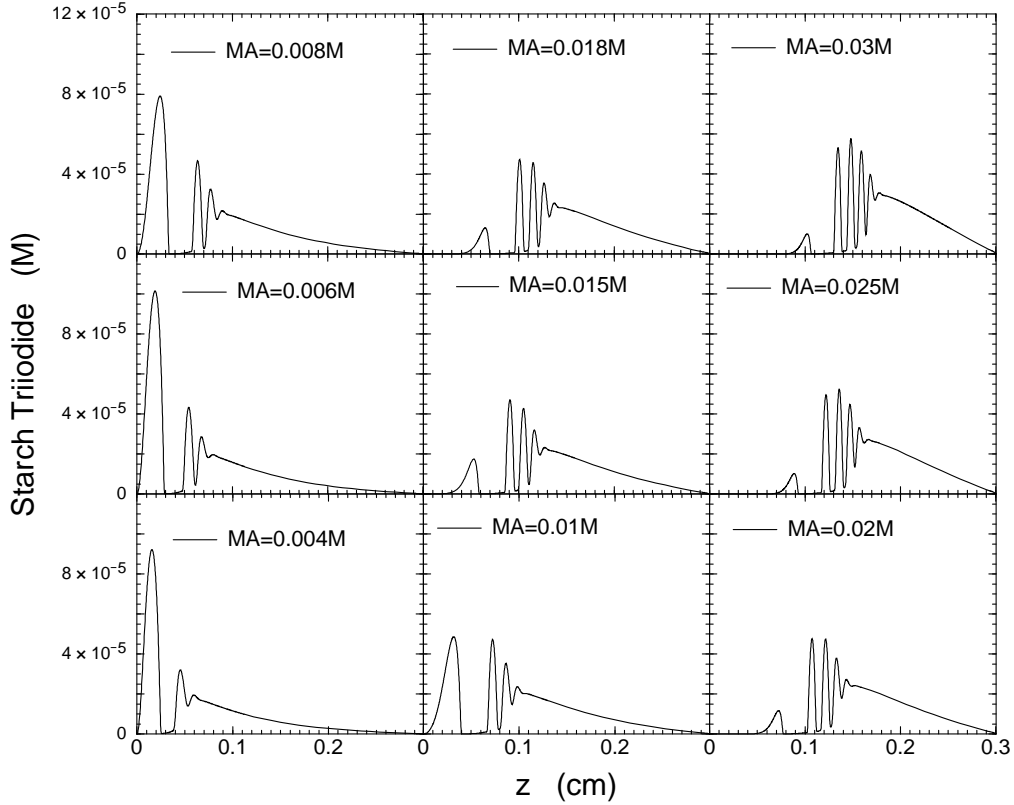


FIG. 10. Stationary solution for $[SI_3^-]$ along feed gradients for various values of malonic acid feed concentration at the left boundary: This series of plots shows how the stationary state along the gradients changes as $[MA]_L$ is varied. The number of peaks in the solution increases with increasing malonic acid concentration, while the left-most peak becomes smaller. The minima correspond to light bands in the experimental results. Instability region I corresponds to stationary states with three peaks, region II with four peaks and region III with five peaks.

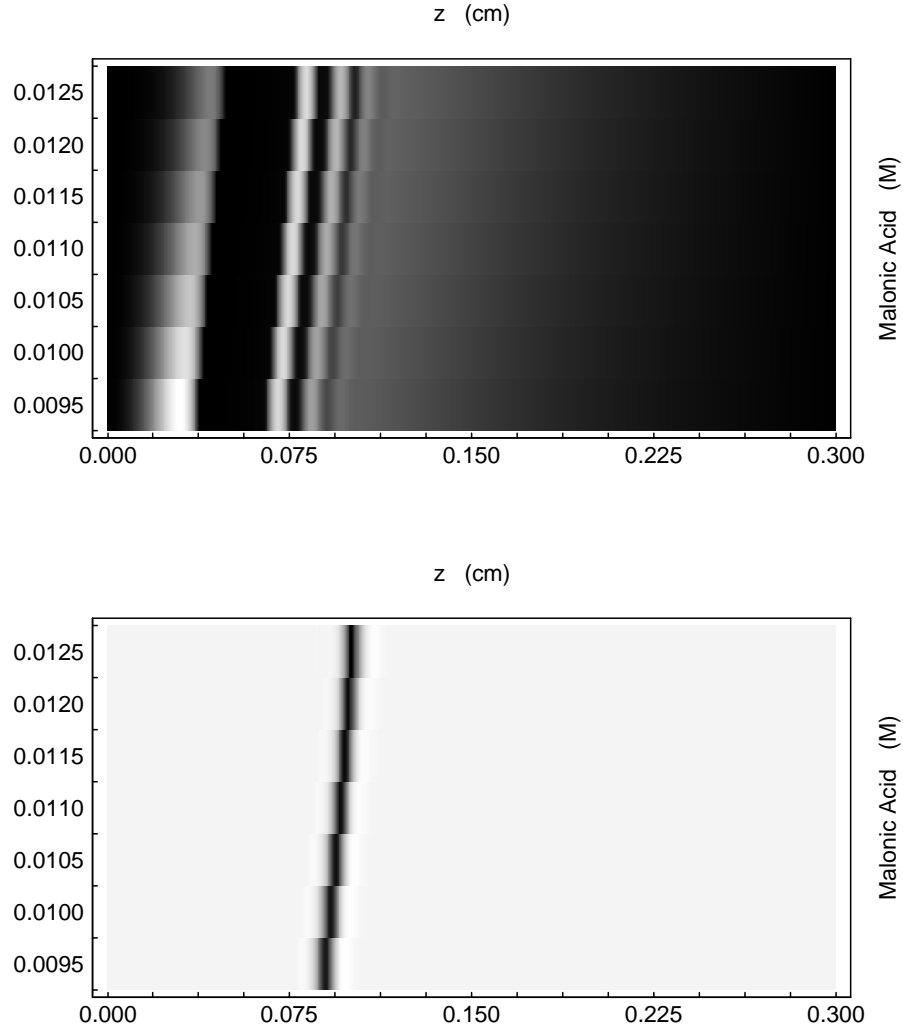


FIG. 11. Density plots of the stationary solution along the gradients and the fastest-growing instability eigenvector for region II: White and black correspond to large and small values of the solution, respectively. The top plot shows the variation of the stationary state in region II with increasing $[MA]_L$. The bottom plot shows how the most linearly-unstable eigenvector is singly peaked and tracks the next-to-last minimum in the solution. (Note: It is difficult to discern the *last* minimum in the top plot.) The “staircase” structure is due to the discrete sampling of $[MA]_L$.

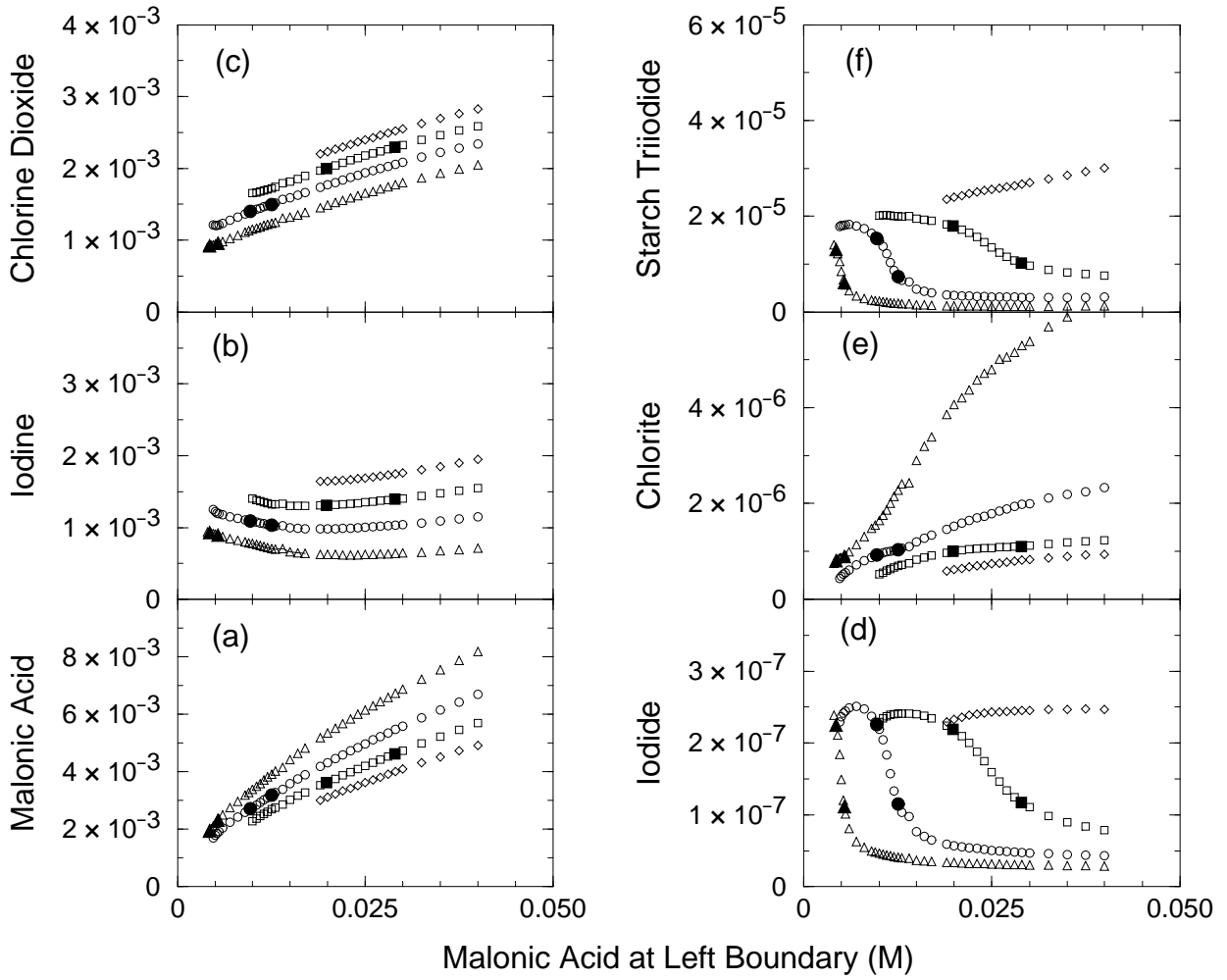


FIG. 12. Values of stationary profiles of the CDIMA chemical species at successive minima of the stationary $[SI_3^-]$ solution as a function of $[MA]_L$: The open triangles, circles, squares and diamonds represent the second, third, fourth and fifth minimum, respectively. The filled symbols correspond to the critical values of $[MA]_L$; the points between the filled symbols correspond to the linearly unstable states. We note that the instability occurs successively along the second, third and fourth minimum. Although the values of $[MA]$, $[I_2]$, $[ClO_2]$ in the unstable ranges continue to increase as functions of $[MA]_L$ in going from one instability region to the next, the trend for the dynamical species $[I^-]$ and $[ClO_2^-]$ is different: the value of $[ClO_2^-]$ remains approximately constant, while $[I^-]$ varies within an approximately constant range.

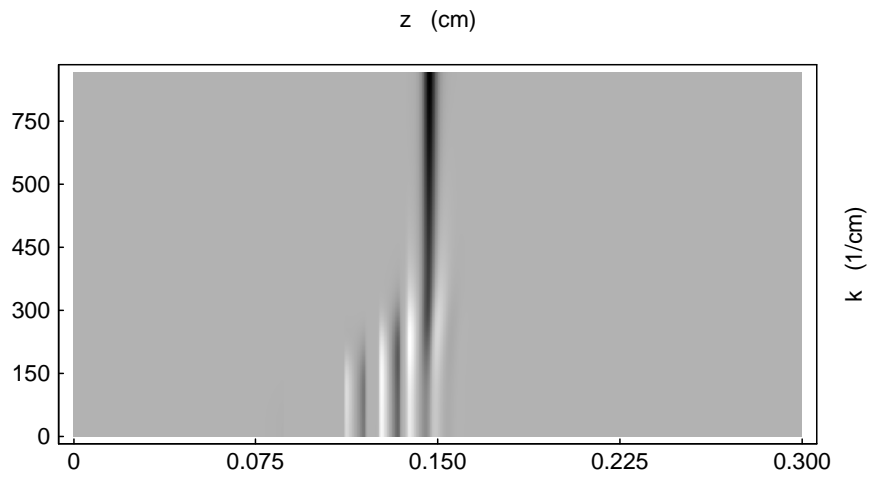


FIG. 13. Density plot of the iodide eigenvector corresponding to the largest eigenvalue as a function of the transverse wave number k and spatial distance along the gradients ($[MA]_L = 0.023$ M): Black and white correspond to low and high values of the eigenfunction, respectively. For small values of k , the eigenvector is multiply peaked while for k larger than approximately 300 cm^{-1} , which includes the unstable range of wave numbers, it is singly peaked.

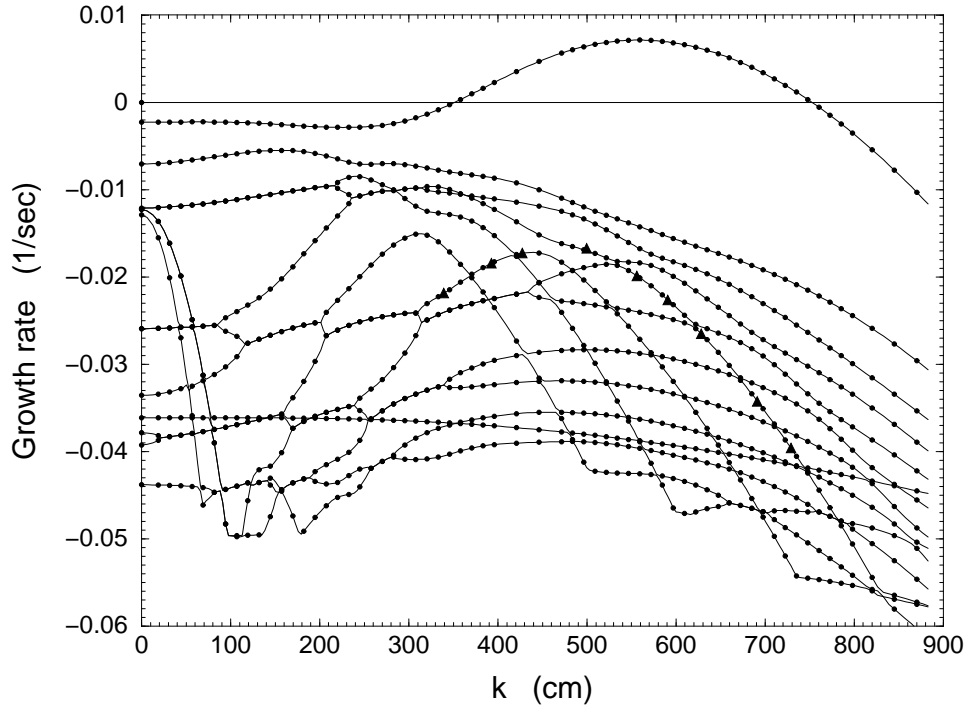


FIG. 14. Spectrum of eigenvalues for $[MA]_L = 0.023$ M: The real parts of the first fourteen eigenvalues with largest real parts have been plotted. The eigenvalues are real, except along intervals where two curves overlap. Some eigenvalue crossings appear imperfect due to the coarse selection of k values. It appears that the first two eigenspectra do not cross but remain distinct. We note that the eigenvalue crossings define distinct “modes” that cut across the spectrum of eigenvalues. The filled triangles indicate the eigenvalues for one such “mode”.

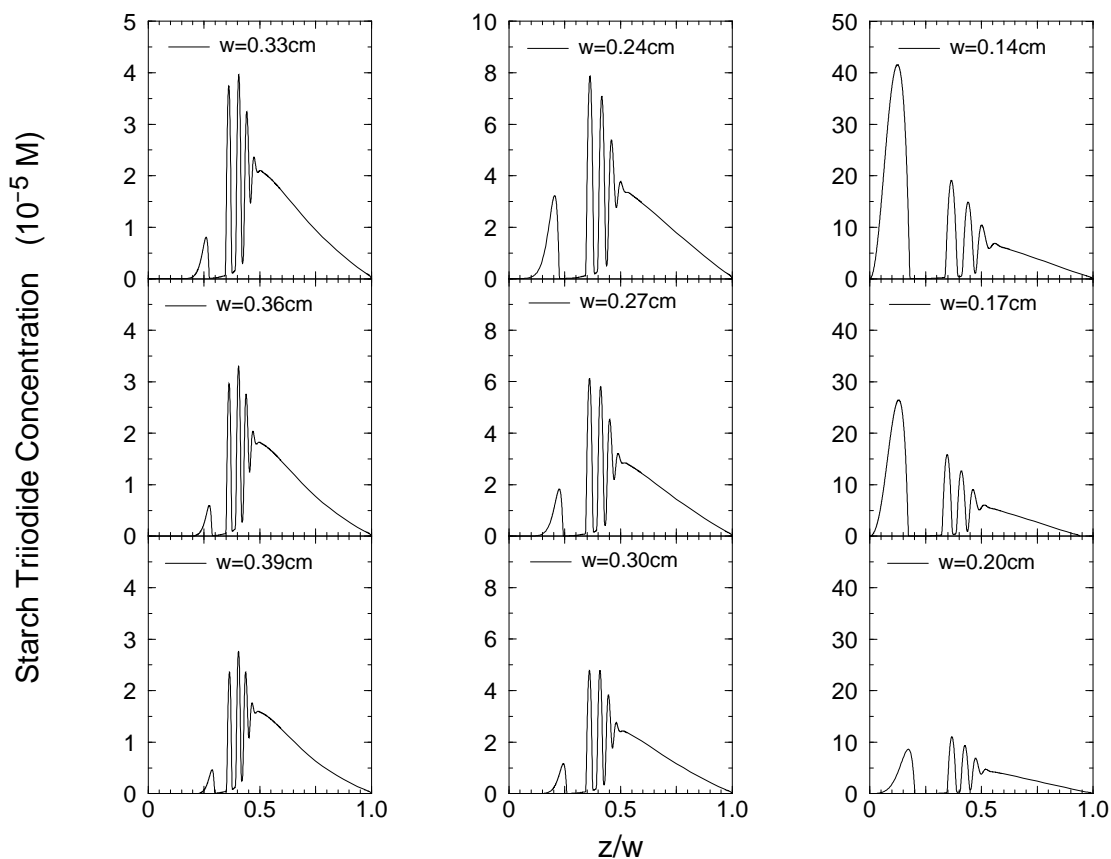


FIG. 15. Stationary solution for $[SI_3^-]$ along feed gradients for various gel widths: This series of plots shows how the stationary state along the gradients changes as the gel width is varied. The horizontal axis is the scaled length along the gradients. With decreasing gel width, we note: (i) shifting of the pattern to the right, and (ii) increase in the concentration scale by approximately an order of magnitude (primarily due to the leftmost peak).

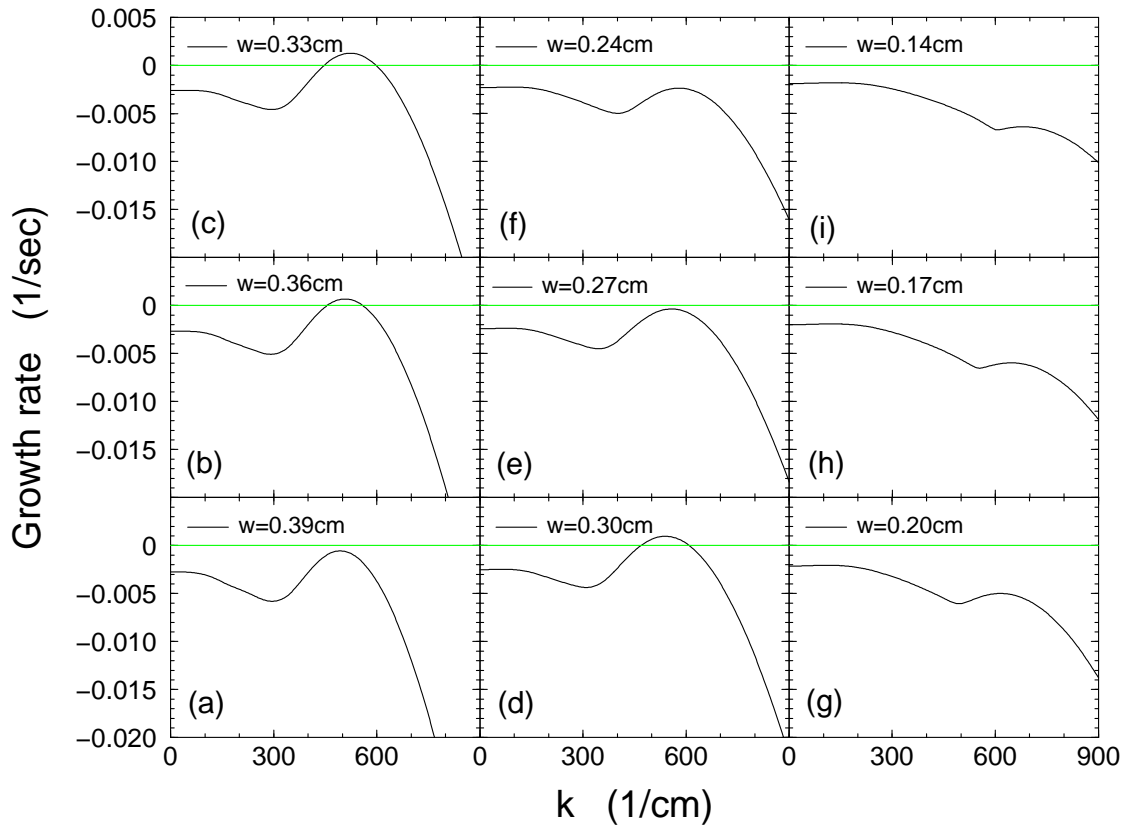


FIG. 16. Gain curve corresponding to largest eigenvalue for various gel widths: (b)-(d) are unstable; in (g)-(i), the largest eigenvalue now occurs at $k = 0$.

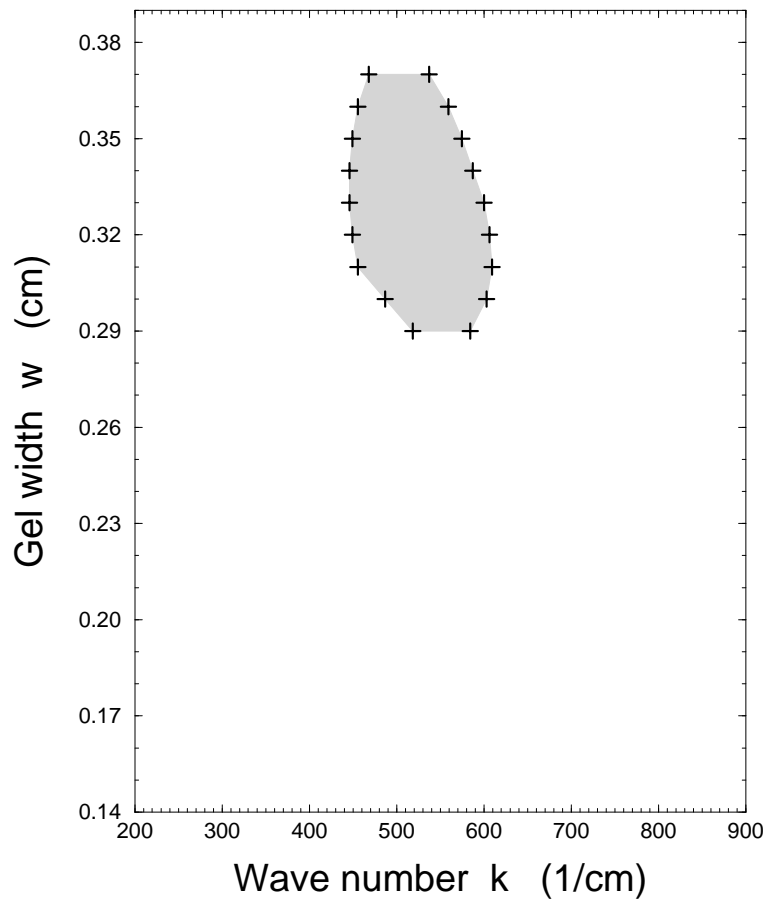


FIG. 17. Gel width w (mm) as a function of wave number k of the transverse instability (1/cm): The crosses represent the marginally stable wave numbers determined from linear stability analysis of the one-dimensional steady states corresponding to the given malonic acid feed concentration. A transverse instability occurs for values of gel width in the shaded regions, with the range of linearly unstable modes delimited by the solid lines for each value of w . The vertical plot range corresponds to the experimental range of gel width in the bevelled thin-strip reactor [14].

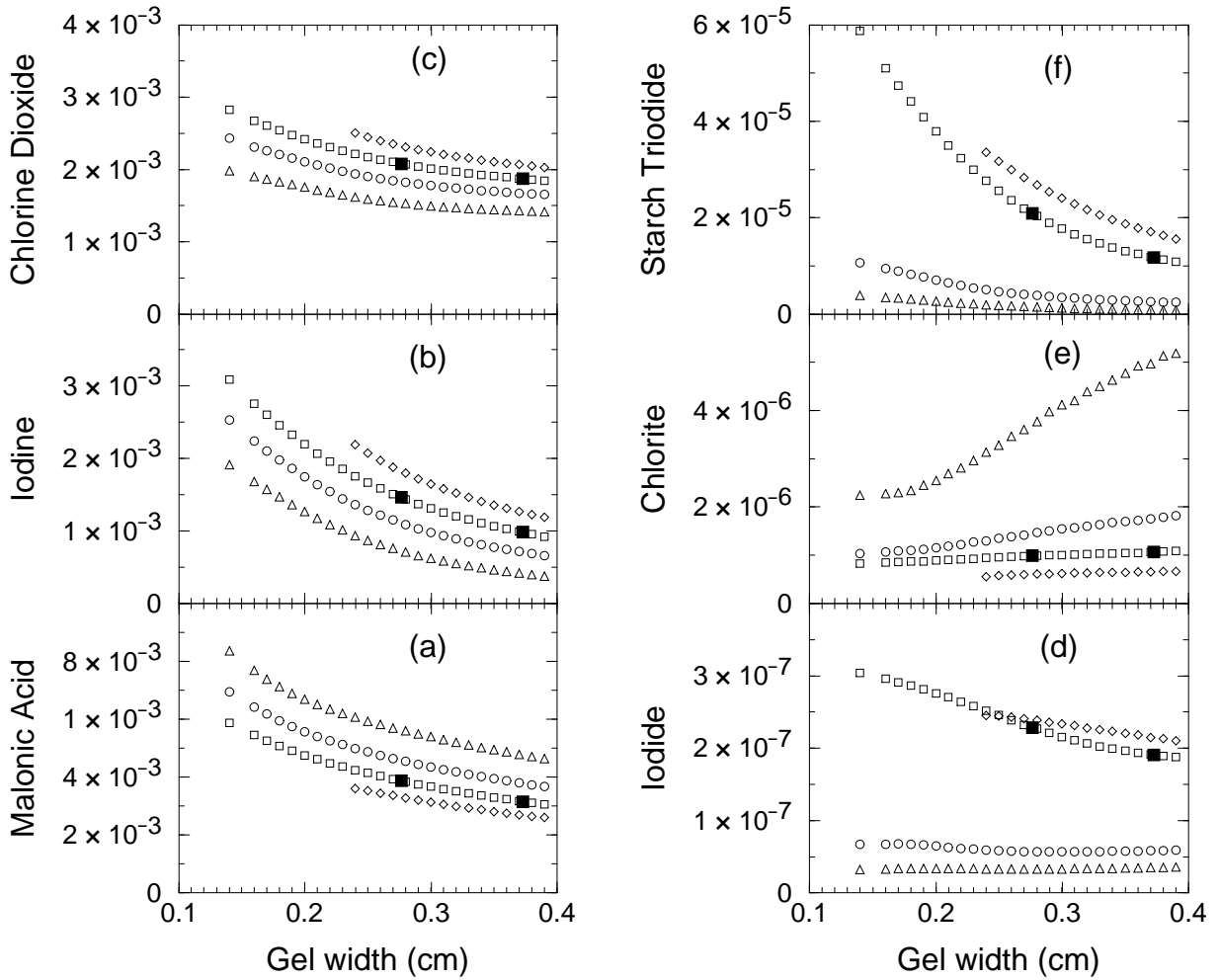


FIG. 18. Values of stationary profiles of the CDIMA chemical species at successive minima of the stationary $[SI_3^-]$ solution as a function of gel width, w : The open triangles, circles, squares and diamonds represent the second, third, fourth and fifth minimum, respectively. The filled symbols correspond to the critical values of gel width; the points between the filled symbols correspond to the linearly unstable states.

TABLE I. Kinetic constants for the CDIMA system.

| Rate or diffusion constant | Dimensions | Value |
|----------------------------|------------------------------------|------------------------------------|
| k_{1a} | (s ⁻¹) | 9×10^{-4} ¹ |
| k_{1b} | (M) | 5×10^{-5} ¹ |
| k_2 | (M ⁻¹ s ⁻¹) | 1×10^3 ¹ |
| k_{3a} | (M ⁻² s ⁻¹) | 1.2×10^2 ¹ |
| k_{3b} | (s ⁻¹) | 1.5×10^{-4} ¹ |
| h | (M ²) | 1.0×10^{-14} ¹ |
| k_+ | (M ⁻² s ⁻¹) | 6.0×10^5 ² |
| k_- | (s ⁻¹) | 1.0 ² |
| D_{I^-} | (cm ² s ⁻¹) | 7.0×10^{-6} ³ |
| $D_{ClO_2^-}$ | (cm ² s ⁻¹) | 7.0×10^{-6} ³ |
| D_{I_2} | (cm ² s ⁻¹) | 6.0×10^{-6} ¹ |
| D_{MA} | (cm ² s ⁻¹) | 4.0×10^{-6} ¹ |
| D_{ClO_2} | (cm ² s ⁻¹) | 7.5×10^{-6} ¹ |
| D_{H^+} | (cm ² s ⁻¹) | 1.0×10^{-5} |
| $K[S]_o$ | (M ⁻¹) | 6.25×10^4 ⁴ |

¹From [19] at 7°C; ²From [17] at 4°C; ³From [16] at 4°C; ⁴From [20] at 4°C.